Devil is in the Defects

Electronic Conductivity in Solid Electrolytes

Gorai, Prashun; Famprikis, Theodosios; Stevanović, Vladan; Canepa, Pieremanuele

DOI
10.1021/acs.chemmater.1c02345

Publication date
2021

Document Version
Final published version

Published in
Chemistry of Materials

Citation (APA)
Gorai, P., Famprikis, T., Stevanović, V., & Canepa, P. (2021). Devil is in the Defects: Electronic Conductivity in Solid Electrolytes. *Chemistry of Materials*, *33*(18), 7484-7498. https://doi.org/10.1021/acs.chemmater.1c02345

CHEMISTRY OF MATERIALS

pubs.acs.org/cm

Article

Devil is in the Defects: Electronic Conductivity in Solid Electrolytes

Prashun Gorai,* Theodosios Famprikis, Baltej Singh, Vladan Stevanović,* and Pieremanuele Canepa*

Cite This: https://doi.org/10.1021/acs.chemmater.1c02345

Read Online

ACCESS | Metrics & More | Article Recommendations | Supporting Information

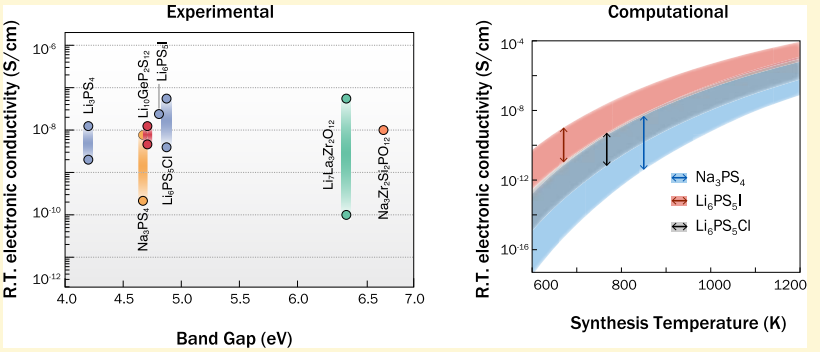

ABSTRACT: Rechargeable solid-state batteries (SSBs) continue to gain prominence due to their increased safety. However, a number of outstanding challenges still prevent their adoption in mainstream technology. This study reveals one of the origins of electronic conductivity, σ_e, in solid electrolytes (SEs), which is deemed responsible for SSB degradation, as well as more drastic short-circuit and failure mechanisms. Using first-principles defect calculations and physics-based models, we predict σ_e in three topical SEs: Li_6PS_5Cl and Li_6PS_5I argyrodites and Na_3PS_4 for post-Li batteries. We treat SEs as materials with finite band gaps and apply the defect theory of semiconductors to calculate the native defect concentrations and associated electronic conductivities. Li_6PS_5Cl, Li_6PS_5I, and Na_3PS_4 were synthesized and characterized with UV−vis spectroscopy, which validates our computational approach confirming the occurrence of defects within the band gap of these SEs. The quantitative agreement of the predicted σ_e in these SEs and those measured experimentally strongly suggests that doping by native defects is a major source of electronic conductivity in SEs even without considering purposefully introduced dopants and/or grain boundaries. We find that Li_6PS_5Cl and Li_6PS_5I are *n*-type (electrons are the majority carriers), while Na_3PS_4 is *p*-type (holes). We suggest general defect engineering strategies pertaining to synthesis protocols to reduce σ_e in SEs and thereby curtailing the degradation mechanism. The methodology presented here can be extended to estimate σ_e in solid-electrolyte interphases. Our methodology also provides a quantitative measure of the native defects in SEs at different synthesis conditions, which is paramount to understand the effects of defects on the ionic conductivity.

1. INTRODUCTION

Rechargeable lithium (Li)-ion batteries have revolutionized the industry of portable devices.[1−3] Concurrently, a daunting task is left to scientists, engineers, and battery manufacturers to develop high-energy-density battery architectures that are safe and cost below 150$/kWh, which could displace combustion engines in favor of more efficient electric ones.[1,3−6] The implementation of large-scale Li-ion technologies is challenged by their low safety.[7−9] Commercial Li-ion batteries contain flammable liquid, nonaqueous organic electrolytes.[7,10] The dynamic nature of the solid-electrolyte interfaces formed at the electrodes and the high flammability of electrolytes set the conditions, together with external events (e.g., the puncturing of the battery casing), for short circuits, thermal runaways, and possible fires.[7,10,11]

Solid-state batteries are considered safer alternatives for energy storage, where liquid electrolytes are replaced by nonflammable solid electrolytes (SEs).[12−17] Although new SEs display record-high Li^+-ion conductivities (>20 mS/cm)[18−22] nearing that of liquid electrolytes (e.g., $LiPF_6$ in ethylene/dimethyl carbonates within tens of mS/cm),[15,23] several challenges in solid-state batteries remain unsolved. These are: (i) the effective passivation of the highly reactive interfaces between the electrodes and the SE,[16,24−31] (ii) the maintenance of physical contact between the electrode and SE over multiple cycles,[16,32] and (iii) the suppression of dendrites—branched filaments of metallic Li growing through SEs and eventually short-circuiting the cells.[29−31,33−38]

Received: July 7, 2021
Revised: August 20, 2021

The nucleation growth of Li dendrites in solid-state batteries drives cell failure.[25,38] Dendrites in SEs and their decomposition products at the interface with electrodes have been linked to an increase in the values of electronic conductivity (σ_e) of solid electrolytes.[16,17,36] The electronic conductivity of specific SEs coupled with their facile Li^+-ion transport may eventually promote the swift recombination of electrons and Li^+ ions into metallic Li, resulting in local nucleation of dendrites.[29,33,35−39] It has been demonstrated that electrolyte decomposition products at both high and low voltages (vs Li/Li^+) may display intrinsic electronic conductivity,[24,25,30,40] whose magnitudes remain elusive.[36,38,41]

While σ_e values are typically reported for completeness, the focus of many reports (e.g., references in Figure 1) shifts

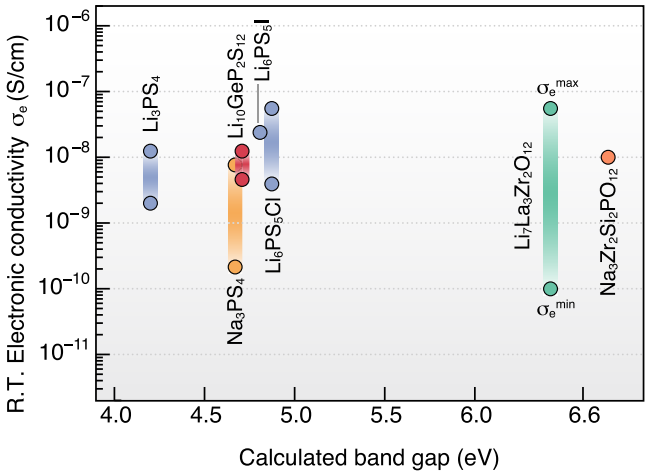

Figure 1. Plot of experimentally reported room-temperature (RT) electronic conductivities σ_e (in S/cm) of SEs vs their experimental and computed band gaps at the GW level of theory. The GW band gap of $Li_7La_3Zr_2O_{12}$ is from ref 42. Vertical bars report the maximum and minimum values of σ_e from the existing reports. σ_e values for $Li_7La_3Zr_2O_{12}$ are from refs 36, 41, $Na_3Zr_2Si_2PO_{12}$,[43] Li_6PS_5Cl,[44,45] Li_6PS_5I,[39] Li_3PS_4,[36,46] and $Li_{10}GeP_2S_{12}$,[18,47] respectively.

entirely to the high intrinsic Li^+-ionic conductivity of novel SE chemistries. Oxide, sulfide, or selenide, and even phosphate and silicate[15] SEs typically display band gaps >4 eV (Figure 1). Thus, the band gap argument, i.e., large band gap materials tend to be good electronic insulators, is often used as a descriptor to indicate low electronic conductivities in SEs.

Nevertheless, from Figure 1, it remains impossible to establish any empirical relationship between values of band gaps (x-axis) and respective experimental values of σ_e (y-axis). If σ_e were to be proportional to the inverse of the band gap, one would expect large band gap materials, e.g., $Li_7La_3Zr_2O_{12}$ (LLZO) or $Na_3Zr_2Si_2PO_{12}$, to exhibit the lowest electronic conductivities, which is not confirmed by the experimental data in Figure 1. Furthermore, the reported values of σ_e for the same SE and with the same nominal composition can surprisingly span several orders of magnitude (Figure 1). This variability is ascribed to a number of factors, including different synthesis procedures, different microstructures, different methods and conditions to measure σ_e, and doping strategies to boost Li-ion conductivities.

A number of recent studies have investigated the issue of electronic conductivity in SEs. Han et al.[36] demonstrated that even electronic conductivities as low as $\sim 10^{-9}$ S/cm can trigger Li dendrite growth. They reported room-temperature σ_e of $\sim 5.5 \times 10^{-8}$ S/cm in LLZO and $\sim 2.2 \times 10^{-9}$ S/cm in Li_3PS_4 and drew the connection to the dendrite growth observed.[36] Dendrites were not observed in the case of LiPON,[36] with σ_e values (10^{-15}−10^{-12} S/cm) at least three orders of magnitude lower than those in LLZO and Li_3PS_4. In striking contrast, recently, Philipp et al.[41] reported σ_e of $\sim 10^{-10}$ S/cm at 293 K in single-crystal Ga-doped LLZO and claimed that such "low" σ_e cannot be responsible for Li dendrite growth in LLZO. These pieces of evidence point to a lack of consensus on the effects of σ_e in SEs.

The emergence of first-principles methods to computationally estimate electronic transport and defect properties offers a practical way to gain insights and quantify the electronic conductivity in SEs. The focus of this work is to: (1) verify quantitatively if the experimentally observed σ_e in SEs can be explained through the formation of bulk charged point defects, and (2) provide a predictive computational framework to estimate σ_e in new SEs, as well as their decomposition products. Here, we modify a methodology based on density functional theory (DFT) calculations combined with a semiempirical model from ref 48 to estimate charge carrier (electron, hole) mobilities. We determine the carrier concentrations and σ_e in three topical SEs: two argyrodites Li_6PS_5X (X = Cl, I) and Na_3PS_4. The latter being important for beyond-Li batteries.[49−53] We identify the most favorable native defects in these SEs that create free electronic charge carriers and give rise to their electronic conductivities. Our methodology also reveals the dominant bulk defects, which influence the ionic conductivity and how the defect concentration can be tuned by adjusting the synthesis conditions. We show that our computational results are consistent with our own experimental results and those in the literature regarding defect populations and electronic conductivity in the investigated solid electrolytes. Notably, the framework of our analysis can account for variations in sample preparation, which could explain the large spread of reported values of electronic conductivity for the same nominal compound in different studies.

These results suggest that even SEs with large band gaps may display appreciable electronic conductivities originating from bulk charged point defects alone. These predictions of σ_e set a lower bound for what can be observed experimentally. The presence of impurity phases and/or extended defects, such as grain boundaries and decomposition phases at the heterogeneous interfaces with the electrodes, may also affect σ_e in real samples. Facile formation of charged defects at the grain boundary may create additional trapped charge carriers, leading to the reduction of Li^+ ions and in-place nucleation of Li metal. We propose defect engineering strategies to control the synthesis to minimize bulk σ_e.

2. POINT DEFECTS AND ELECTRONIC CONDUCTIVITY

Crystalline solids contain defects at finite temperatures that range from native point defects, extrinsic impurities to grain boundaries.[54] Atomic-scale point defects are present in metals, semiconductors, and insulators under virtually all conditions. The most common native (intrinsic) point defects include vacancies, antisites, and interstitials. For example, in Li_6PS_5I, three types of native point defects can occur and are investigated here: (i) vacancies, e.g., Li vacancy (V_{Li}), (ii) interstitials, e.g., Li interstitial (Li_i), and (iii) antisites, e.g., sulfur on iodine antisite (S_I); symbols in parentheses denote

https://doi.org/10.1021/acs.chemmater.1c02345
Chem. Mater. XXXX, XXX, XXX−XXX

the defects in Kröger−Vink notation. Point defects can be charged (ionized), which may create free carriers—electrons or holes—in the material. Such free carriers will give rise to electronic conductivity. Therefore, to understand and quantify electronic conductivity, one must first determine the thermodynamics of point defect formation. Importantly, here, we treat SEs as materials with finite band gaps.[55,56] As such, the defect theory developed for semiconductors can be applied to calculate the defect energetics in SEs.[56−58]

2.1. Defect and Carrier Concentration. Within the supercell approach,[59] the formation energy $\Delta E_{D,q}$ of a point defect D in charge state q is

$$\Delta E_{D,q} = [E_{D,q} - E_{host}] + qE_F + \sum_i n_i\mu_i + E_{corr} \quad (1)$$

where $[E_{D,q} - E_{host}]$ denotes the total energy difference between the undefected supercell of the SE with no net charge (E_{host}) and the supercell with defect D and charge q. The term qE_F is the energy of exchanging the charge q with the reservoir of charges described by the Fermi energy (E_F). n_i is the number of atoms of element i added ($n_i > 0$) or removed ($n_i < 0$) to create the defect D. μ_i is the chemical potential of element i. Thus, the term $\sum_i n_i\mu_i$ accounts for the energy associated with the exchange of elemental species. Equation 1 describes the defect formation in the grand-canonical ensemble accounting for the exchange of both charge and elemental species with an external reservoir. These terms are calculated from first-principles using periodic supercells, which introduce artifacts arising from finite-size effects. Corrections to the formation energy are lumped into E_{corr} (Section 6).

For a given SE, one calculates the defect formation energy $\Delta E_{D,q}$ for all types of defects of interest in all plausible charge states (q). The results are presented in the form of a "defect diagram"; examples are shown in Figure 4. The x-axis is the Fermi energy (E_F), spanning from the valence band maximum (VBM) to the conduction band minimum (CBM). E_F is conventionally referenced to the VBM, which is set to 0.0 eV. Since $\Delta E_{D,q}$ is linear with respect to E_F (eq 1), $\Delta E_{D,q}$ is a straight line with slope q, the charge state of the defect. A donor defect is one with a positive slope (positively charged defect), and an acceptor has a negative slope. Charge neutral defects appear as horizontal lines. For a given defect, only the lowest-energy-charged state at a certain E_F is shown. As such, a change in the slope of the line for a given defect represents the value of E_F where the energetically most favorable charge state changes —this crossover point is the charge transition level. Importantly, the defect formation energy is a function of the elemental chemical potential (μ_i), which is determined by the chemical or electrochemical environment (Section 3.1).

Under specific synthesis conditions, the equilibrium E_F is set by a charge balance between the charged defects (donors, acceptors) and charge carriers (electrons, holes). A Boltzmann distribution regulates the defect concentration such that $[D_q] = N_s e^{-\Delta E_{D,q}/k_B T}$, where $[D_q]$ is the defect concentration, N_s is the lattice site concentration where the defect D can be formed, k_B is the Boltzmann constant, and T is the temperature. At a given temperature, the concentration of charge carriers depends only on E_F, as per the Fermi−Dirac distribution. When the charges are balanced, the total positive charges are equal to the negative charges. The charge neutrality conditions can be solved self-consistently to determine the equilibrium E_F and the corresponding defect and carrier concentrations. The net free carrier concentration is $|n_e - n_h|$, where n_e and n_h are electron and hole concentrations. If $n_e > n_h$, the material is n-type and p-type when $n_h > n_e$.

In our treatment, we assume that the defects formed at the synthesis temperature are kinetically "frozen in", that is, when a material is quenched to a lower temperature (e.g., room temperature), the defect concentrations reflect the defect chemistry at the synthesis temperature. This widely used assumption emanates from the fact that most defects are not mobile, i.e., the kinetic barrier for motion is large at lower temperatures. Hence, the defect concentrations reflect the equilibrium synthesis conditions. Defects such as Li interstitials that are mobile even at room temperature may not re-equilibrate at the lower temperature because the material needs to maintain charge balance. This is especially applicable if Li interstitials are shallow defects. Throughout this study, we assumed the synthesis temperature to be 800 K, which is a typical condition for Li_6PS_5X argyrodites and Na_3PS_4.[60,61]

To maintain charge balance, the net electronic carrier (electrons, holes) concentration also reflects the synthesis conditions. However, the *free* carrier concentrations may change if deep defects are present—the electronic charge is trapped in these defect states and their availability as "free" carriers will depend on the temperature and the energy separation of defect states and the relevant band edges, e.g., donor(acceptor) states and conduction(valence) band edge. Since electronic carriers are mobile even at lower temperatures, they can undergo "re-equilibration" at RT in a way that the sum of the trapped and free electronic charges remains unchanged. Morgan and collaborators calculated the RT re-equilibrated electronic carrier concentrations in $Li_7La_3Zr_2O_{12}$, where deep defects are present in high concentrations.[62]

2.2. Electronic Conductivity. In the framework of the Drude theory,[63] the electronic conductivity (σ_e) is proportional to the concentration of free charge carriers (n, electrons or holes) and their mobility (ζ). One can estimate σ_e by knowing n and ζ using eq 2

$$\sigma_e = ne\zeta \quad (2)$$

where e is the electronic charge. Assuming that free carriers arise from the formation of charged point defects, we can estimate n as a function of the synthesis conditions.

The intrinsic, phonon-limited carrier mobility is the upper limit of mobility and can be determined accurately with *ab initio* methods by computing the electron−phonon coupling matrix,[64] but such calculations are still computationally prohibitive. To circumvent the direct calculations of ζ, one may adopt a computationally more tractable method. Some of us have previously developed a semiempirical model to estimate ζ by fitting measured room-temperature ζ and parameters calculated from DFT calculations.[48] Assuming band conduction, the phonon-limited carrier mobility is modeled as

$$\zeta = A_0 B^s (m_b^*)^{-t} \quad (3)$$

where B is the bulk modulus, and m_b^* is the band-effective mass of the SE. A_0, s, and t are constants that were obtained in ref 48 by fitting eq 3 to experimentally measured room-temperature values of ζ. Therefore, to estimate ζ using eq 3, we compute B and m_b^*, both of which can be calculated accurately with DFT. Details on the calculation of B and m_b^* are in Section 6. Since the computed ζ is the intrinsic upper limit, the estimated σ_e must be treated as the upper limit as well, assuming that there are no additional sources for generating or

https://doi.org/10.1021/acs.chemmater.1c02345
Chem. Mater. XXXX, XXX, XXX−XXX

capturing/recombining electronic carriers besides the bulk charged point defects.

3. RESULTS

3.1. Phase Equilibria of Li_6PS_5X (X = Cl or I). For a given material, the accessible range of elemental chemical potentials in eq 1 is constrained by the condition of its phase stability. The prevailing elemental chemical potential, i.e., $\mu_{element}$ in eq 1, is controlled by the specific synthesis conditions of the SE and/or the operating electrochemical conditions of the cell as in real experiments. The provenance of each compound and its respective polymorphs computed for the construction of the phase diagrams are reported in Table S4 of the Supporting Information (SI). In general, Li(Na)-rich and Li(Na)-poor conditions may promote Li(Na) uptake or loss in/from SEs but are most likely to drive chemical transformations as indicated by the phase diagrams of Figure 2 and Figure S5 in SI.

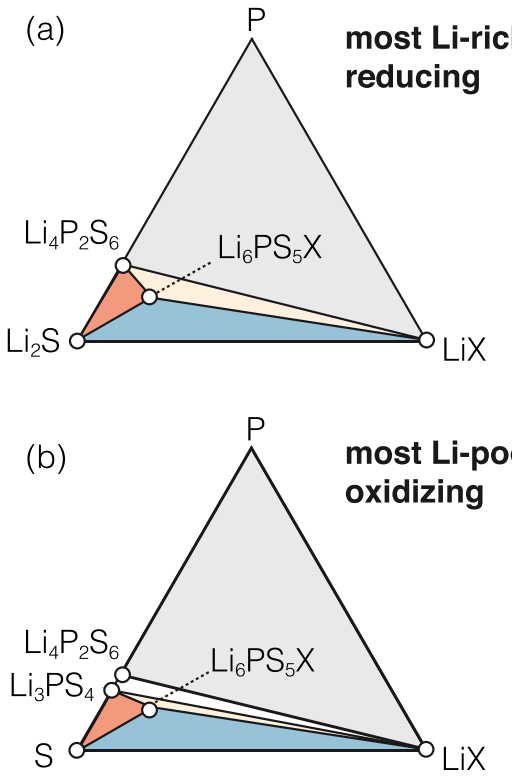

Figure 2. Projected compound phase diagrams showing the phase equilibria of argyrodite Li_6PS_5X with X = Cl and I in the quaternary Li-P-S-X chemical space. Projections are shown for specific Li chemical potentials: (a) most Li-rich or reducing conditions, and (b) most Li-poor or oxidizing conditions. Equilibrium tie lines are drawn between the argyrodite and the neighboring competing phases. The colored triangles set the limits of elemental chemical potentials in eq 1.

As an example, we discuss the phase stability of Li_6PS_5X with X = Cl and I, and this can be extended to Na_3PS_4 (Section S4 of the Supportive information). Figure 2 shows projections of the computed compound quaternary Li-S-P-X phase diagrams at specific electrochemical conditions. Figure 2a corresponds to the most Li-rich conditions under which Li_6PS_5X are thermodynamically stable. This also corresponds to the thermodynamic stability of Li_6PS_5X in a highly reducing environment. Figure 2b shows the phase stability of Li_6PS_5X for the most Li-poor and, simultaneously, the most S-rich (in this case, equilibrium with elemental S) conditions capturing the stability of Li_6PS_5X at higher voltages. The values of the elemental chemical potentials for the phase stability of Li_6PS_5I, Li_6PS_5Cl, and Na_3PS_4 are listed in Tables S1, S2, and S3 in the SI. Although $Li_2P_2S_6$ is experimentally reported[65] and is considered in the construction of the phase diagram in Figure 2, $Li_2P_2S_6$ is predicted to be metastable (0.017 eV/f.u. above the convex hull) in DFT.

The three-phase regions (triangles) formed by the phases in equilibrium with Li_6PS_5X set the accessible range of chemical potentials. Indeed, in Figure 2a Li_6PS_5X is connected by tie lines with a number of compounds, including Li_2S, Li_2PS_3, and LiX (Cl or I). These findings are in line with previous experimental and theoretical reports.[24,25,30,66] Notably, Figure 2a indicates that Li_6PS_5X cannot be in direct equilibrium with Li metal (low voltages). Instead, Li_6PS_5X is in equilibrium with the Li-rich phase Li_2S. Thus, the three-phase region formed by Li_2S, $Li_4P_2S_6$, and Li_6PS_5X is important to study the types of point defects and charge carriers, as well as their concentrations when Li_6PS_5X is subjected to low voltages vs Li/Li^+. From Figure 2a, we also infer that all argyrodite-type SEs are unstable at low voltage, i.e., Li/Li^+ −3.04 V vs SHE, as also reported previously.[24,25,30]

At oxidizing conditions, Li-poor conditions, or equivalently higher voltages vs Li/Li^+, two important stability regions for Li_6PS_5X are identified: (i) the three-phase region formed by S-Li_3PS_4-Li_6PS_5X, corresponding to S-rich conditions (equilibrium with elemental S), and (ii) the LiX-S-Li_6PS_5X corresponding to the most X-rich conditions. Notably, the low boiling point of sulfur (~445 °C) may create S-poor conditions during the synthesis of sulfide-based SEs, and consequently, introduce defects that readily form under S-poor conditions. For these reasons, syntheses of sulfide-based SEs are in some cases performed in excess of sulfur.[30,67,68] For example, Zeier and co-workers used 3 wt % excess sulfur to compensate for sulfur loss at higher temperatures during the synthesis of $Li_{10}Ge_{1-x}Sn_xP_2S_{12}$.[67,68] Similarly, an argyrodite-type Li_7GeS_5Br was grown with 6 mol % excess S.[69]

A byproduct of plotting the equilibrium phase diagrams of Figure 2a,b are the thermodynamic stability windows of Li_6PS_5X—the voltage range within which Li_6PS_5X is thermodynamically stable. We find that Li_6PS_5I and Li_6PS_5Cl have limited electrochemical stability windows (Tables S1 and S2 in Supporting Information) of ~0.278 and 0.290 V, in agreement with previous reports on Li_6PS_5Cl (~0.3 V).[24,25,30] These Li(Na)-rich and Li(Na)-poor conditions are to be considered the highest and lowest potentials at which these SEs are stable. More positive and more negative potentials will cross the cathodic or anodic stability windows of the SEs, leading to their decomposition.

3.2. Band Gaps of Li_6PS_5X and Na_3PS_4. In eq 1, the defect formation energy ($\Delta E_{D,q}$) and the defect and charge carrier (electron, hole) concentrations are sensitive to the electronic structure of the material, particularly the band gap. We computed the band gaps of Li_6PS_5X using the GW approximation (Section 6), which is the state-of-the-art for calculating the electronic structures of semiconductors and insulators,[70] and has been previously used in battery research.[42,71] It is well documented that the GW approximation provides more accurate electronic structures, including band gaps, of semiconductors and insulators.[72−74] Our GW

https://doi.org/10.1021/acs.chemmater.1c02345
Chem. Mater. XXXX, XXX, XXX−XXX

band gaps of Li_6PS_5Cl and Li_6PS_5I are 4.86 and 4.80 eV, respectively, and 4.67 eV for the tetragonal-Na_3PS_4.

To study the electronic properties of Li_6PS_5Cl, Li_6PS_5I, and Na_3PS_4 and to provide an assessment of the computational approach, diffuse-reflectance ultraviolet-visible (UV−vis) spectra were collected for these materials, as shown in Figure 3a.

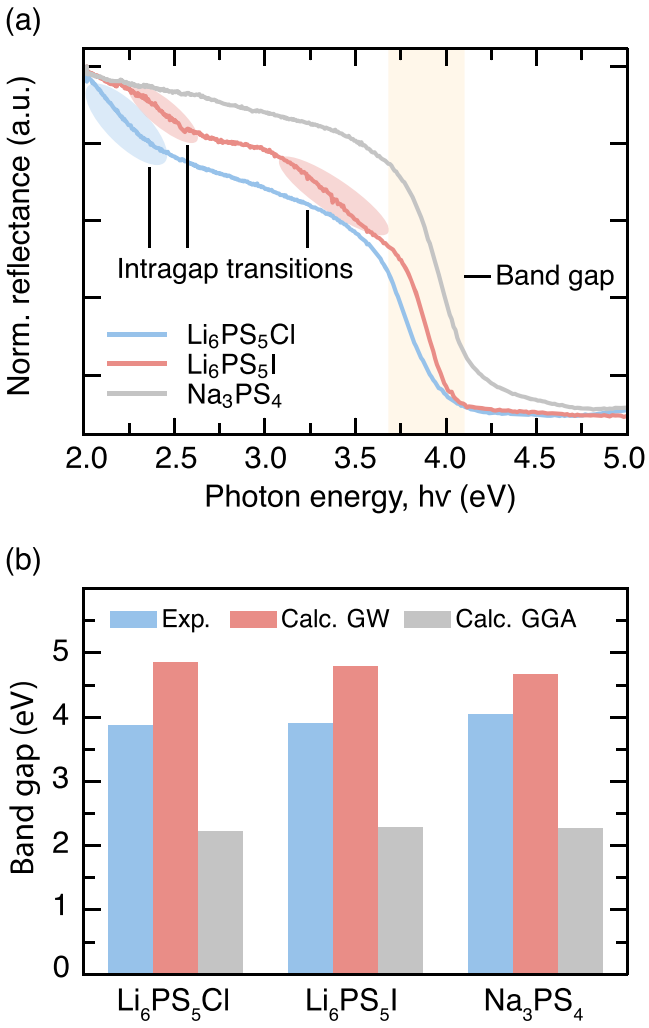

Figure 3. (a) UV−vis reflectance spectra of sulfide solid electrolytes featuring characteristic band gap transitions ~4 eV and intragap transitions at energies <4 eV. (b) Comparison of the experimentally determined optical band gaps and the calculated electronic band gaps from GGA (PBE) and GW (Section 6). The determination of band gaps and their comparisons with the scarce literature on this topic is provided in Table S5.

The quality of the Li_6PS_5Cl, Li_6PS_5I, and Na_3PS_4 samples was determined using X-ray diffraction as detailed in Section 6.5. X-ray diffraction patterns and the Rietveld refinements are shown in Section S10.

The spectra collected for all samples featured sharp step-wise changes in the wavelength region around ~300 nm, indicative of the optical band gap of approximately ~4 eV in all three materials, namely, 3.88, 3.91, and 4.05 eV for Li_6PS_5Cl, Li_6PS_5I, and Na_3PS_4, respectively. From the combination of the calculated electronic band structures (Section S11) and experimentally observed shape of the absorbance spectra transformed by the Tauc equation, we conclude that all three materials considered here can be regarded as direct-band-gap semiconductors exhibiting Γ−Γ transitions. The detailed procedure on the experimental determination of band gaps is presented in Section S8.

For the two argyrodites Li_6PS_5Cl and Li_6PS_5I in Figure 3a, we observe additional reflectance (absorption) edges besides the band gap at lower energies. These observations are in line with the results presented in the dissertation of Kong,[75] who also observed "multiple absorption edges" for various lithium argyrodites. This behavior points to the presence of intragap states that can be attributed exactly to the same defects that are the object of the present study (see below). Our preliminary measurements show that Na_3PS_4 can also exhibit such intragap states as a function of synthesis protocol (Figure S11). The connection to the calculations is made in Section S9 of the SI, providing a preliminary framework for the identification and quantification of these defects by UV−vis spectroscopy in future work.

Figure 3b compares the experimentally determined band gaps with the calculated values using the GW approximation and standard GGA-PBE functional.[76] For all three materials considered, the experimentally determined values lie between the ones routinely calculated in the literature with GGA-PBE and the GW calculations in this work. However, in all three cases, the overestimation of GW remains significantly smaller than the underestimation of GGA (nearly 50%), as compared to the experimental values, validating our approach. If the band gap calculated with GW is indeed slightly overestimated, the carrier concentrations, and therefore, σ_e are expected to be even higher than our predictions exposed in Section 3.3.

3.3. Native Defect Chemistry of Argyrodites. We begin by analyzing the energetics of defect formation in argyrodites Li_6PS_5X (X = I, Cl). The formation energies of native point defects ($\Delta E_{D,q}$) in Li_6PS_5Cl are plotted as a function of the Fermi energy E_F (Section 2) in Figure 4. Since $\Delta E_{D,q}$ depends on the elemental chemical potentials (eq 1), we examine the defect formation energetics under the limiting synthesis conditions: most Li-rich or reducing and most Li-poor or oxidizing (Section 3.1). The dominant defects are those with the lowest $\Delta E_{D,q}$ at the equilibrium Fermi energy, $E_{F,eq}$ (vertical dashed line in Figure 4). The slope of each line represents the corresponding charge state of the defect.

Under both Li-rich (reducing) and Li-poor (oxidizing) conditions, the dominant defects are Li interstitials (Li_i) and anion antisites (S_{Cl}, Cl_S). In calculating the defect energetics, all symmetry nonequivalent Wyckoff sites for each defect type are considered. In Figure 4, only the Wyckoff site with the lowest $\Delta E_{D,q}$ is shown. The defect energetics of all Wyckoff sites are provided in Figure S1 of the SI. While the dominant defects are the same under the most Li-rich and Li-poor conditions, their formation energies are different under each condition.

In a SE, it is expected that Li interstitials and/or vacancies are among the lowest formation energy defects. We find that Li_6PS_5Cl also contains appreciable concentrations of anion antisite defects, S_{Cl} and Cl_S, which suggests that Li_6PS_5Cl is prone to anion site disorder. At a synthesis temperature of 800 K, S_{Cl} and Cl_S concentrations are 2.6×10^{19} cm^{-3} and 1.9×10^{19} cm^{-3} under the most Li-rich conditions (Figure 4a). Recent experimental studies have confirmed anion site disorder in Li_6PS_5Cl and Li_6PS_5Br.[60,77,78] These experimental findings are in excellent agreement with our predictions, thus providing further confidence in our calculated defect energetics. Sulfur vacancies (V_S) are present in much lower concentrations

https://doi.org/10.1021/acs.chemmater.1c02345
Chem. Mater. XXXX, XXX, XXX−XXX

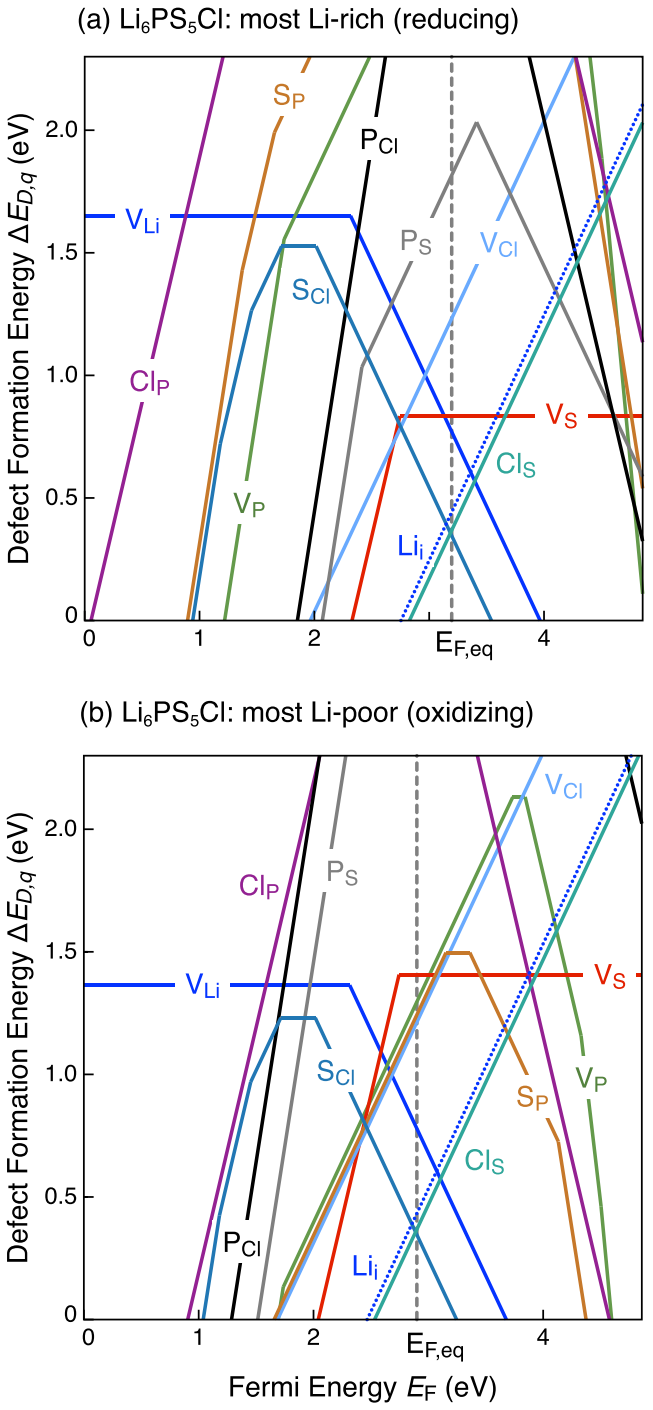

Figure 4. Formation energy of native point defects ($\Delta E_{D,q}$) in Li_6PS_5Cl as a function of Fermi energy (E_F) under the (a) most Li-rich and (b) most Li-poor conditions within the phase stability region (Figure 2). E_F is referenced to the valence band maximum. The upper limit of E_F shown is the conduction band minimum such that E_F values range from 0.0 eV to the band gap. Different Wyckoff sites for each defect type are considered. For clarity, only the Wyckoff site with the lowest $\Delta E_{D,q}$ is shown. The equilibrium Fermi energy ($E_{F,eq}$), marked by the dotted vertical line, is calculated at 800 K.

compared to lithium interstitial (Li*i*). For instance, under Li-rich conditions, V_S concentration (2.2×10^{16} cm^{-3}) is ~300 times smaller than the Li_i concentration (6.6×10^{18} cm^{-3}) at 800 K.

The defect energetics of Li_6PS_5Cl set the equilibrium Fermi energy ($E_{F,eq}$) above the mid-gap (see vertical dashed lines in Figure 4a,b). Consequently, Li_6PS_5Cl is a native *n*-type material with excess free electrons. The free electron concentration is the highest when Li_6PS_5Cl is synthesized under the most Li-rich (also, most S-poor, Figure 4a) conditions and lowest when grown under the most Li-poor (also, S-rich, Figure 4b) conditions. Assuming a typical synthesis temperature of 800 K, the free electron concentration is bounded between 6.0×10^6 cm^{-3} (Li-poor) and 3.7×10^8 cm^{-3} (Li-rich).

The defect chemistry of Li_6PS_5I (Figures S2 and S3) is qualitatively and quantitatively different from that of Li_6PS_5Cl—the lowest-energy defects are Li_i and V_{Li}, with much lower concentrations of V_I, and anion antisites S_I and I_S. The Li_i concentration in Li_6PS_5I (~1.6×10^{18} cm^{-3}) is about half an order of magnitude lower than in Li_6PS_5Cl (~6.6×10^{18} cm^{-3}) at Li-rich conditions, which can be gleaned by comparing Figure 4 to Figure S2a. Kraft et al.[60] established a direct link between the concentration of Li_i^+ defects and the prefactor in the Arrhenius expression of the Li^+-ion diffusivity, showing that the more defective Li_6PS_5Cl has a larger prefactor and higher Li^+-ion conductivity than Li_6PS_5I, which is also in excellent agreement with our calculations. In contrast to Li_6PS_5Cl, anion antisites in Li_6PS_5I (S_I, I_S) are present in lower concentrations suggesting the absence or low degree of anion disorder. This picture is also consistent with a recent study[60] that confirmed the absence of anion disorder in Li_6PS_5I.

Although the defect concentrations are lower in Li_6PS_5I, the concomitant free electron concentration is ~30 times higher compared to Li_6PS_5Cl. At 800 K, the free electron concentration is bound between 2.0×10^8 cm^{-3} for Li-poor and 1.1×10^{10} cm^{-3} for Li-rich conditions, respectively.

3.4. Native Defect Chemistry of Na_3PS_4. The formation energies of native defects in tetragonal Na_3PS_4 are shown under the limiting growth conditions—most Na-rich (reducing, Figure S4a) and most Na-poor (oxidizing, Figure S4b). The limiting conditions correspond to vertices of the phase stability region of Na_3PS_4 (Table S3), where $\Delta\mu_{Na}$ is the highest (Na-rich) and the lowest (Na-poor).

Under the most Na-rich (most S-poor) synthesis conditions, the lowest-energy defects in Na_3PS_4 are Na vacancy (V_{Na}), Na interstitial (Na_i), and S vacancy (V_S), with V_{Na} and Na_i concentration being ~4.1×10^{16} cm^{-3} at 800 K (V_{Na} concentration is slightly higher than Na_i). The equilibrium Fermi energy ($E_{F,eq}$) calculated at 800 K is marked in Figure S2. In contrast, under the most Na-poor (S-rich, equilibrium with elemental sulfur), the lowest-energy defects are V_{Na} and S_{Na} antisite defects, such that their concentration is ~2.9×10^{18} cm^{-3} at 800 K.

Under Na-poor synthesis conditions, Na interstitial (Na_i) concentrations are approximately 2 orders of magnitude lower (~5.6×10^{14} cm^{-3}) than under Na-rich conditions. Conversely, the V_{Na} concentration under Na-rich conditions is 2 orders of magnitude lower than under Na-poor conditions. Unlike the argyrodites, $E_{F,eq}$ is pinned below the mid-gap, and consequently, Na_3PS_4 is a *p*-type material with free hole concentrations bound between 1.1×10^6 cm^{-3} (Na-rich) and 3.2×10^9 cm^{-3} (Na-poor).

3.5. Predicted Electronic Conductivity of Li_6PS_5X and Na_3PS_4. Here, we estimate the room temperature (300 K) electronic conductivity of Li_6PS_5X and tetragonal Na_3PS_4 due to the formation of charged point defects. The electronic

https://doi.org/10.1021/acs.chemmater.1c02345
Chem. Mater. XXXX, XXX, XXX−XXX

Table 1. Comparison between the Predicted Range of Room-Temperature σ_e and Experimental Values of σ_e (in S/cm)[a]

SE	ζ_e	ζ_h	predicted σ_e	experimental σ_e	
Li_6PS_5I	35.6	1.6	$(0.12-6.28) \times 10^{-8}$	2.4×10^{-8}	ref 39
Li_6PS_5Cl	24.9	0.7	$(0.02-1.48) \times 10^{-9}$	$5.1 \times 10^{-9}/5.2 \times 10^{-8}$	refs 44, 45
Na_3PS_4	9.5	2.6	$(0.004-13.1) \times 10^{-10}$	2.14×10^{-10}	ref 79

[a]SE carrier mobilities (in $cm^2/(V\ s)$) computed with the model of eq 3. ζ_e (ζ_h) is the room-temperature intrinsic electron (hole) mobility.

conductivity is a function of the synthesis conditions (specifically, the elemental chemical potentials) and other physical variables, such as the synthesis temperatures. To quantify σ_e, we need to estimate the room-temperature carrier mobility (ζ) using the semiempirical model of eq 3. The computed electron (ζ_e) and hole (ζ_h) for each SE are presented in Table 1.

Using the values of ζ, we computed the electronic conductivities at room temperature (Table 1). As expected, σ_e increases with temperature —a direct consequence of the increase in the free or net carrier concentration $|n_e - n_h|$. Considering the error of ±1/2 order of magnitude in the estimation of the carrier mobility (ζ),[48] the predicted σ_e values are also accurate within ±1/2 order of magnitude (eq 2), which is well below the variability observed in the experimental data of Figure 1.

Figure 5 and Table 1 present the computed σ_e of the three SEs as a function of synthesis temperature. Note the majority of charge carriers in argyrodites are electrons, while in Na_3PS_4, they are holes (*p*-type). Combined with a high ζ_e, Li_6PS_5I displays the highest σ_e among the three SEs (Table 1).

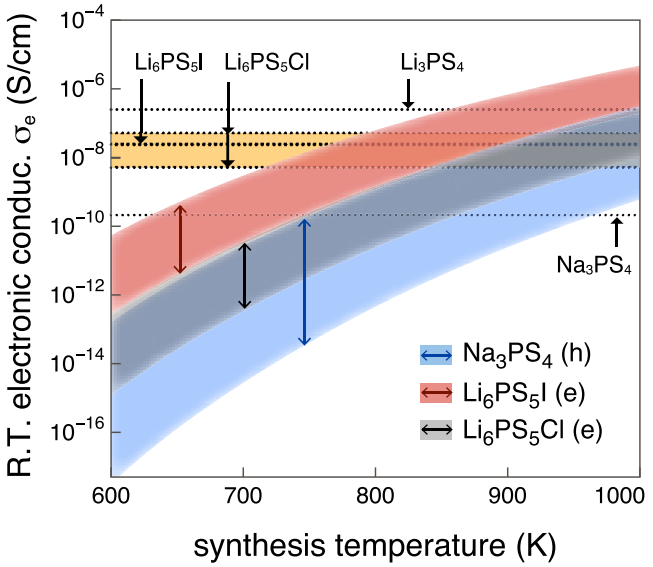

Figure 5. Computed room temperature (RT) electronic conductivity (σ_e) as a function of the synthesis temperature for three SEs: tetragonal Na_3PS_4, argyrodites Li_6PS_5I, and Li_6PS_5Cl. The range of σ_e at any given temperature is set by the range of elemental chemical potentials (synthesis conditions) and denoted by a colored band for each electrolyte. For reference, the experimentally measured electronic conductivities are shown for Li_3PS_4 (2.5×10^{-7} S/cm),[36] Li_6PS_5I (2.4×10^{-8} S/cm),[39] and Li_6PS_5Cl (5.1×10^{-9} to 5.2×10^{-8} S/cm) yellow shaded region,[44,45] and Na_3PS_4 (2.1×10^{-10} S/cm).[79] The position of the arrows is a guide for the eye of the experimental values of electronic conductivities. The typical synthesis temperature of argyrodites Li_6PS_5X (X = Cl, I) is 823 K, while that of Na_3PS_4 is 773 K. Li_3PS_4 is synthesized at room temperature but using high-energy ball milling, and as such, the local temperatures are unclear.

In Table 1, the computed values of σ_e are either in good agreement or slightly underestimated compared to the experimental values, which suggests that the experimental measurements of σ_e include additional sources of charge carriers beyond native point defects. The experimentally measured value by Boulineau et al.[39] falls within the range of the predicted σ_e. The predicted range of σ_e for Li_6PS_5X (X = I, Cl) indicates that depending on the synthesis conditions, at a specific synthesis temperature, it can vary by a factor of 75, with lower σ_e values obtained when the argyrodite is synthesized under Li-poor conditions or oxidative environments. The variation in σ_e is expected to be even larger when considering the additional effect of differences in synthesis temperatures.

When one compares the lower limits of electronic conductivities between Li_6PS_5Cl and Li_6PS_5I, the computed σ_e for Li_6PS_5Cl is on average ~40 times lower than Li_6PS_5I (at 800 K). The experimentally reported values,[44,45] for Li_6PS_5Cl (~5.1×10^{-9} to 5.2×10^{-8} S/cm), are shown as a yellow shaded region in Figure 5 and appear slightly higher than the range of computed values.

In the case of Na_3PS_4, we find much lower values of σ_e compared to Li_6PS_5X. The reduction of σ_e in Na_3PS_4 originates from a combination of the lower hole mobility (ζ_h, Table 1) and lower free hole concentrations when compared to the argyrodites. Na_3PS_4 also shows the largest range of variability among the three SEs at any given temperature (>4 orders of magnitude assuming synthesis at ~800 K, Figure 5).

Notably, this data suggest that in argyrodite-type SEs, the lowest value σ_e is achieved when the material is synthesized under alkali-poor/S-rich conditions, and the highest σ_e under alkali-rich/S-poor conditions. These conditions also correspond to oxidative/high-voltage and reducing/low-voltage conditions, respectively. An inversion in trend is observed for Na_3PS_4, where the lowest σ_e is attained under alkali-rich/S-poor synthesis conditions, comparable to low voltages vs Na/Na^+.

4. DISCUSSION

Previous investigations of native defects in SEs have emphasized strategies to improve ionic conductivity.[55−57,80,81] In this study, we focus on *all* native defects that may alter the concentration of charge carriers (electrons, holes), in addition to ionic carriers, i.e., Li^+ and Na^+ ions. In a previous study,[56] we found V_{Li} + Li_i Frenkel pairs to be unstable in $Li_{10}GeP_2S_{12}$ such that Li_i spontaneously relaxes into the neighboring V_{Li}. By extension, we expect Frenkel pairs to be unstable in similar thiophosphate materials Li_6PS_5X and Na_3PS_4. A deeper understanding of native defects is crucial to rationalize the possible sources of intrinsic electronic conductivities in SEs. Here, we propose a general model to estimate the electronic conductivity in bulk SEs. We have applied this model to predict the electronic conductivities of three topical sulfide-

https://doi.org/10.1021/acs.chemmater.1c02345
Chem. Mater. XXXX, XXX, XXX−XXX

based SEs, i.e., Li_6PS_5Cl, Li_6PS_5I, and Na_3PS_4.[14,17] As demonstrated extensively in previous reports,[14,17,28,31,36,82−85] grain boundaries might provide an additional source of charge carriers, and hence, introduce additional complexity when attempting to systematically understand the crucial role of native point defects in giving rise to electronic conductivity.

4.1. Influence of Synthesis and Electrochemical Conditions on Native Defect Formation. The synthesis conditions of solid electrolytes can be tuned to facilitate or curtail the formation of specific types of native defects. The physical and chemical parameters, such as temperature and the elemental chemical potentials, are mostly set by the synthesis protocols (e.g., high-temperature solid-state, soft solution-based, or mechanochemical-synthesis as in ball milling), which can greatly influence the formation of specific defects and lead to appreciable variations in the electronic properties of SEs.[86] High-temperature synthesis as well as sintering treatments, such as spark-plasma can not only contribute to significant increase and variation of native point defects but also extended defects. For instance, high-temperature treatments may alter the grain boundary morphology in SEs and their microstructures.[83]

Notably, different synthesis strategies can be adopted to target the same crystallographic phase of interest, but each strategy may create distinct defect types depending on the synthesis conditions.[86] For example, our preliminary UV−vis measurements on mechanochemically prepared Na_3PS_4 samples clearly indicate the effect of ball-milling parameters on the concentration of mid-gap defect states (Figure S11). Thus, in computing the dominant native defects, we have carefully considered these aspects. Throughout the discussion, we assumed that the equilibrium temperature (at which defects form) is the typical synthesis temperature ∼800 K (∼527 °C) of the SEs studied here.[44]

We have identified the important regions of the phase diagram of these SEs that correspond to actual synthesis conditions. The phase diagrams are important to study the selected electrochemical environments that the SE may experience at specific voltages set by the electrodes (Figure 2), which provide an understanding of the types of defects that can be formed under an applied bias (as discussed in Section 3.1). An applied voltage is a sufficiently large energy to trigger the decomposition of the SE at the electrodes and form entirely new phases, as noticed in previous experimental and theoretical reports.[24,25,30,40,66] In addition, simple contact between electrodes and SEs can drive energetic chemical reactions. For example, simply pressing Li metal on Li_6PS_5X (with X = Cl, Br and I), Wenzel et al.[66] could verify the formation of Li_2S, LiX, and Li_3P via X-ray photoemission spectroscopy.

Aware of the important role the structural disorder can play in influencing the electronic structure and defect properties of Li_6PS_5X,[56,87] here, we have undertaken a statistical ensemble approach[88] to create representative "ordered" structures. Through a sampling of 831 and 1847 structures of Li_6PS_5I and Li_6PS_5Cl, respectively (Section 6), we identified the representative structures that were then utilized for calculating the electronic structure and defect formation energetics. The tetragonal Na_3PS_4 is a fully ordered phase.[61]

The accurate prediction of specific defects relies on the determination of accurate band gaps in these SEs, which is pivotal to identify the charge carrier concentrations and eventually electronic conductivities. The band gaps were computed using the state-of-the-art GW methodology, which have previously not been reported in the literature. The GW band gaps of Li_6PS_5X and Na_3PS_4 are all >4.7 eV. The GW band gaps are considerably larger than those computed with standard GGA-PBE exchange−correlational functional (e.g., 2.27 eV for tetragonal Na_3PS_4, 2.24 eV for Li_6PS_5Cl and 2.29 eV in Li_6PS_5I, respectively) and with range-separated HSE06 hybrid functional (3.49 eV in Na_3PS_4), which are frequently adopted as the standard methods in this community. These predictions were confirmed by UV−visible measurements with band gaps of 3.88, 3.91, and 4.05 for Li_6PS_5Cl, Li_6PS_5I, and Na_3PS_4, respectively (Figure 3 and Table S5). The good agreement between our theoretical and experimentally determined band gaps provides confidence in our methodology. The computed band gaps of argyrodites are comparable to that of $Li_{10}GeP_2S_{12}$ (∼4.6 eV),[56] with both structures containing P-S moieties.

Unsurprisingly, our results suggest that both Li and Na vacancies as well as their interstitials are among the favorable defects that form in both Li_6PS_5X and Na_3PS_4, thereby enabling their high ionic conductivities.[30,39,44,57,61,89,90] In the case of the Li_6PS_5X, we find that the chemical environments, either Li-poor or Li-rich, do not substantially alter these defect concentrations. Importantly, these chemical environments can also be accessed at specific electrochemical conditions: a Li(Na)-rich condition represents the situation of the electrolyte placed near a highly reducing material and mimicked by the low voltage of the Li(Na)-metal electrode (Figure 2a). The electrochemical environment felt by SEs near a high-voltage cathode material (e.g., voltage > 3.0 V vs Li/Li^+) is well captured by the Li(Na)-poor conditions (Figure 2b).

Although Li_6PS_5X is unstable against Li-metal anodes and decomposes into Li_2S, Li_3P, and LiX as in Figure 2,[66] these materials can be safely studied against more positive voltage anodes, e.g., LiIn alloys (∼0.6 V vs Li/Li^+). Therefore, the Li-rich situations, where the μ_{Li} is set by Li_2S, Li_3P, and LiX (Figure 2a), are representative of the environment set by a higher voltage anode compared to Li metal.

In striking contrast, Na vacancies and interstitial defects appear abundant in the Na_3PS_4 but only in Na-rich (low voltages vs Na/Na^+) and sulfur-poor conditions. While the high volatility of sulfur during certain synthesis conditions may create S-defective electrolytes, our data suggest that sulfur loss during synthesis is beneficial to the formation of Na vacancies and interstitials that facilitate Na^+-ion transport. In the context of this study, we also find that under Na-rich conditions, the electronic conductivity (σ_e) is minimized (Section 3.5). Although from these findings the synthesis of Na_3PS_4 under Na-rich conditions appears beneficial to enhance the ionic- and lower the electronic conductivities, a direct control of the Na availability (μ_{Na}) during synthesis might not be most practical. However, controlling the anion species, e.g., S (μ_S), appears less challenging and is regularly applied.

In Li_6PS_5Cl, antisite defects (S_{Cl} and Cl_S) appear favorable and with non-negligible concentrations (-10^{19} cm^{-3} at ∼800 K). Our observations are in line with experimental X-ray diffraction studies on Li_6PS_5Cl, where site disorder on Cl and S sites is observed.[60,91] In line with our findings, Gautam et al.[77,92] have also shown that an accurate control of the synthesis parameters in a similar argyrodite Li_6PS_5Br material can directly affect the Br-S site disorder and Li defects.

From the relatively high concentrations $\sim 10^{16}$ cm^{-3} of antisite defects (i.e., S_I and I_S) computed in Li_6PS_5I, we

https://doi.org/10.1021/acs.chemmater.1c02345
Chem. Mater. XXXX, XXX, XXX−XXX

speculate that similar antisite defects may manifest in the I-based argyrodite but may fall below the detection limit of X-ray analysis.

Recently, Minafra et al.[91] proposed that the X/S site disorder is associated with spatially diffuse Li^+ distributions, which agrees well with the higher concentrations of V_{Li} and Li_i in Li_6PS_5Cl. In Na_3PS_4, antisite defects S_{Na} are expected to be present in higher concentrations under Na-poor conditions.

Therefore, we show that for specific defects, there is a strong dependence on the chemical, and especially the electrochemical environment, i.e., voltage. However, it remains to be verified experimentally whether specific voltages can vary the type of defect locally in the SE, especially at the electrode/electrolyte interfaces. Our model does not capture polarization effects of the electrolyte/electrode interfaces or the effect played by decomposition phases that may form at the electrode.[24,25,93] Similar predictions can be extended to chart the electronic properties of the decomposition phases forming at the electrode/electrolyte interfaces to infer their intrinsic electronic conductivities and their role in battery degradation.

4.2. Defect Engineering of Electronic Conductivity in Solid Electrolytes. The position of $E_{F,eq}$ determines the defect and carrier concentrations. In the case of Li_6PS_5Cl (Figure 4a,b), the $E_{F,eq}$ is pinned between 3.2 and 3.4 eV with respect to the valence band maximum. $E_{F,eq}$ lies in the vicinity of the intersection of V_{Li}^{1-}, Li_i^{1+}, and V_I^{1+}. Since $E_{F,eq}$ is pinned above the mid-gap, Li_6PS_5I is an n-type conductor and the free electron concentration ranges between 10^8 and 10^{10} cm^{-3} depending on the electrochemical conditions. Likewise, Li_6PS_5Cl is an n-type conductor. While Li_6PS_5Cl can accommodate larger defect concentrations than Li_6PS_5I, its electron concentration ($\sim 10^6-10^8$ cm^{-3} at ~800 K) remains ~30-fold lower than in Li_6PS_5I. The experimentally measured σ_e[39,45] for Li_6PS_5I and Li_6PS_5Cl are 2.4×10^{-8} and 5.1×10^{-9} to 5.2×10^{-8} S/cm, respectively, which are within the range of predicted σ_e (Figure 5). While a range of values has been measured in Li_6PS_5Cl, the scarcity of measured σ_e values for Li_6PS_5I prevents us from making comparative conclusions. Our estimated σ_e suggests that the measured value for Li_6PS_5I (2.4×10^{-8} S/cm) might be the lower limit. In contrast, Na_3PS_4 appears as a native p-type material when synthesized at ~800 K with predicted hole concentrations $\sim 1.1 \times 10^6$ and 3.2×10^9 cm^{-3} under Na-rich and Na-poor conditions, respectively.

We estimate the phonon-limited *intrinsic* carrier mobility (ζ) using a semiempirical model.[48] Typically, ζ is limited by ionized-impurity scattering only at lower temperatures when the material is moderately doped, either natively or with extrinsic dopants. For example, ζ in silicon above temperatures of ~50 K is dominated by electron−phonon scattering.[94] Therefore, it is reasonable to assume that ζ in SEs is limited by phonon scattering. Additional scattering mechanisms, e.g., disorder scattering, may also limit mobility, but it is not explicitly considered in calculating ζ.

With the free carrier concentrations calculated from defect calculations and ζ calculated with the semiempirical model, we could then estimate the electronic conductivities of Li_6PS_5X and Na_3PS_4 (Figure 5). The computed band gaps (all >4.6 eV) follow the order Li_6PS_5I > Li_6PS_5Cl > Na_3PS_4 (Figure 5). Given that the electron binding energies in I are lower than in Cl, it is expected to observe $\sigma_e(Li_6PS_5I) > \sigma_e(Li_6PS_5Cl)$. Nevertheless, the scarcity of experimental reports of σ_e warrants future verification of these hypotheses.[39,44,45]

The electronic conductivity in SEs is routinely measured by two methods: (i) the Hebb-Wagner polarization and (ii) DC polarization. Riess[95] showed that the application of the two-electrode Hebb-Wagner method to mixed ionic-electronic conductors is clearly limited. Instead, a four point Hebb-Wagner-type or van der Pauw setups ensure that the experimental conditions are correct.[95] These setups are commonly used to measure carrier mobilities in materials for solid-oxide fuel cells, thermoelectrics, and photovoltaics,[96−100] but may not always be suitable for SEs due to their innate chemical reactivity with specific electrode materials (e.g., Li and Na-metal). Given that our models highlight intrinsic electronic conductivities in SEs, the determinations of σ_e via DC polarization or Hebb-Wagner measurements remain extremely delicate, especially if the selectivity of the ion or electron-blocking electrodes are not adequate. Measurements of σ_e in SEs should be carefully performed and following rigorous protocols, which are currently lacking.

We now discuss strategies to control the electronic conductivity by defect engineering of Li_6PS_5X argyrodites. Figure 6 displays the computed and experimental σ_e as a function of synthesis temperature. From Figure 6, the upper bound of σ_e is set by the Li-rich conditions, whereas the lower bound by Li-poor regimes. At ~800 K, the upper and lower bounds account for 60× and 50× change in σ_e of Li_6PS_5Cl and Li_6PS_5I, respectively. The experimental values of σ_e (dotted line for Li_6PS_5I in Figure 6a and shaded yellow region for Li_6PS_5Cl in Figure 6b) are qualitatively captured by our predictions. From these observations, we can devise practical and general strategies to reduce σ_e in SEs:

1. For electron (n-type) conductors, such as argyrodites, syntheses in Li-poor and oxidizing conditions are advised. In contrast, for hole (p-type) conductors, e.g., Na_3PS_4, lower electronic conductivities are achieved under reducing environments (i.e., Na-rich conditions). While we show that optimal synthesis conditions can minimize the electronic conductivity of specific carrier types (electrons or holes), from a practical standpoint, it is not clear what is the best way to accurately control the μ_{Na} during a reaction.
2. The direct link between σ_e and temperature clearly suggests that the implementation of soft-chemistry protocols as opposed to typical high-temperature synthesis should be sought. Although mechanochemical syntheses, e.g., ball milling, are commonly parked under "low-temperature methods", the local effective temperatures experienced by the material can range within hundreds of °C.[101−103] Likewise, sintering procedures for material densification (especially in oxide SEs including LLZO and NaSICONs) should be cautiously applied.[83] In particular, the concentration of defects also depends on postsynthesis cooling protocols,[77,92] and quenching techniques may "freeze in" existing defects at high temperatures, in contrast to slow cooling methods, enhancing defect re-equilibration.
3. Soft-chemistry synthesis protocols should be considered to prevent the loss of volatile elements (e.g., sulfur) from the samples. We showed that materials unintentionally grown under S-poor conditions might lead to higher undesired σ_e in Li_6PS_5X.[67,68]
4. Controlling the loss of active elements, i.e., Li and Na during syntheses remain more delicate and intimately

https://doi.org/10.1021/acs.chemmater.1c02345
Chem. Mater. XXXX, XXX, XXX−XXX

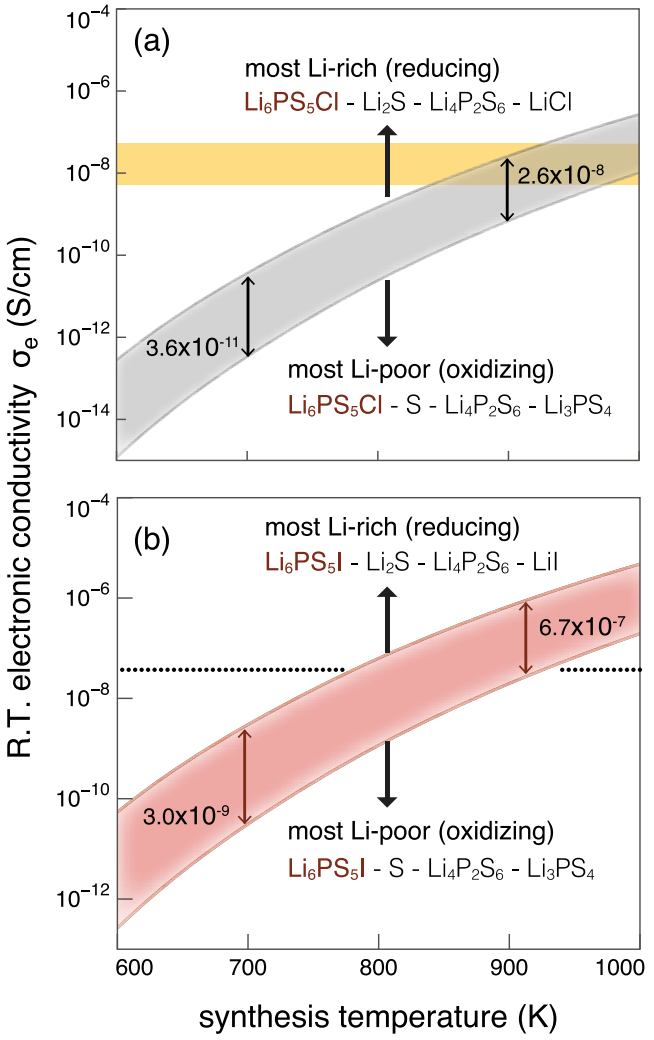

Figure 6. Predicted range of room temperature (RT) electronic conductivity (σ_e) in (a) Li_6PS_5Cl and (b) Li_6PS_5I as a function of the synthesis temperature and the chemical environment. The upper bound of σ_e is set by the Li-rich (reducing) conditions in the phase diagram (Figure 2a), whereas the lower bound is by the Li-poor or oxidizing conditions. The yellow shaded region in (a) is the experimentally observed range of σ_e in Li_6PS_5Cl (Figure 5). The experimental value of $\sigma_e = 2.4 \times 10^{-8}$ S/cm in (b) is from ref 39. The change in σ_e between the upper and lower bound are shown with arrows at selected temperatures (700 and 900 K).

connected to the nature of charge carriers in specific SEs. Specifically, in electron conductors, such as Li_6PS_5X, Li-loss will suppress the overall electronic conductivity, whereas in *p*-type conductors (e.g., Na_3PS_4) Na loss will unpleasantly increase σ_e.

5. Therefore, we could envisage employing defect engineering techniques such as phase-boundary mapping, as applied in thermoelectrics,[104] to precisely control or tune the elemental chemical potentials during synthesis, and consequently, regulate the defect/carrier concentrations, and σ_e.
6. Another possible strategy to decrease σ_e involves low-temperature annealing to re-equilibrate the defects. However, there are challenges with this approach. First, only mobile defects, e.g., alkali ions (interstitials) and vacancies, may re-equilibrate, whereas the concentrations of defects with significant kinetic barriers for diffusion will remain unchanged. Second, the equilibrium at lower temperatures will lead to lower alkali ion concentrations (following a Boltzmann distribution) and possibly lower ionic conductivity.
7. We showed that the local electrochemical conditions are dictated by the electrode potentials, which affect the charge carrier concentrations, and σ_e. Further investigations are needed to elucidate this specific aspect.

These considerations are of general applicability and can be extended to other electrolytes. These design rules may also be suitably modified when developing electrode coating materials, whose specific requirements may be different.[105−108] It is worth commenting that although accurate band gaps are crucial to identify the equilibrium Fermi energy, and hence, the type and concentrations of electronic charge carriers, the magnitude of the band gap alone cannot be used as a proxy to comment on the severity (or lack thereof) of electronic conductivity in specific SEs.

5. CONCLUSIONS

A central problem in the development of solid-state batteries is the detrimental intrinsic electronic conductivity that contributes to dendrite growth and, at worst, to the short-circuiting of the battery. In this study, we reveal using first-principles calculations that the native defects are the source of the observed electronic conductivities in the three topical SEs, i.e., Li_6PS_5Cl, Li_6PS_5I, and Na_3PS_4. UV−vis measurements could attest to the band gap of these SEs and could elucidate the formation of intragap transitions, which could be linked to intrinsic defects. We quantitatively establish the range of electronic conductivities in these SEs. We leverage this knowledge to propose defect engineering strategies for tuning the defects and, therefore, charge carriers and electronic conductivity. Clearly, electronic conductivity should be minimized, but there will inherently be a tradeoff between minimizing this quantity and ionic conductivity, phase purity, etc. It is yet unclear what level of electronic conductivity is acceptable for solid electrolytes in batteries, and the answer to that question will also likely depend on the microstructure and materials properties of the active materials as well as cycling parameters. Further work is required to extend the models and the methodologies presented in this study to more complex scenarios such as oxide-based electrolytes, where extended defects (e.g., grain boundaries) may affect electronic conductivity, as well as interphases between solid electrolyte and electrode materials. Unraveling the origin of electronic conductivity in SEs should be a primary goal for the community. To that end, we believe that rigorous and systematic protocols should be developed to measure electronic conductivity.

6. METHODOLOGY

6.1. Structure Selection for Defect Calculations. In this study, we perform defect calculations on the high-Na^+-conductivity and fully ordered polymorph of Na_3PS_4, which arranges into a tetragonal crystal structure ($P\bar{4}2_1c$, see Figure S3).[61] A cubic phase of Na_3PS_4 ($I\bar{4}3m$) also exists.[61] The crystal structure of tetragonal Na_3PS_4 is composed of PS_4^{3-} polyhedra arranged in a body-centered-cubic-like manner with two unique Na Wyckoff sites (4d, 2a), and one each for P(2a) and S(8e).

https://doi.org/10.1021/acs.chemmater.1c02345
Chem. Mater. XXXX, XXX, XXX−XXX

Unlike Na_3PS_4, Li argyrodites Li_6PS_5X (X = Cl, Br, I) exhibit structural disorder, including partial site occupancy. The site disorder in Li_6PS_5X was modeled with an ensemble statistical procedure, and as discussed in Section S5 in the SI.[56] A disordered macrostate can be expressed as a thermodynamic average of structurally ordered microstates.[87,88] The identification of the symmetrically distinct orderings in Li_6PS_5X was performed using the method proposed by Hart and Forcade.[109] We identified 831 and 1847 distinct orderings in the unit cells of Li_6PS_5X. For performing defect calculations, we chose the most probable structures marked in Figures S5 and S6 (Supporting Information).

6.2. Calculation of Defect Formation Energy. First-principles calculations are used to compute the formation energies of native defects as functions of the Fermi energy. We calculate the defect formation energies in Na_3PS_4 and Li_6PS_5X (X = Cl, I) using DFT and a standard supercell approach.[59] Within the supercell approach, the formation energy ($\Delta E_{D,q}$) of a point defect D in charge state q is calculated as in eq 1

In eq 1, μ_i is the chemical potential of element i and n_i is the number of atoms of element i added ($n_i < 0$) or removed ($n_i > 0$) from the supercell. E_F is the Fermi energy. qE_F is the characteristic energy of exchanging charge between the defect and the reservoir of charge, the Fermi sea. The supercell approach to predict defect energetics suffers from artifacts due to finite-size effects.

Various correction schemes are available to correct for the finite-size artifacts and inaccurate electronic structure and are factored as E_{corr} in eq 1.[59] Additional artifacts are introduced due to the limitations of DFT, most notably, the underestimation of the band gap with standard functionals, such as in the generalized gradient approximation (GGA) of Perdew–Burke–Ernzerhof (PBE).[76]

Among the native defects, we considered vacancies, antisites, and Li and Na interstitials, with each unique Wyckoff site treated as a different defect. For each defect, charge states q = −3, −2, −1, 0, 1, 2, 3 are calculated; for some defects, such as V_P, additional charge states q = −5, −4, 4, and 5 are also calculated. The possible sites for Li and Na interstitials are determined by a Voronoi tessellation scheme as in pylada-defects.[110] In each structure, the energetically most favorable interstitial configuration is assessed by relaxing up to 15–20 different possible interstitial configurations.

The total energies of the supercells are calculated using the GGA-PBE functional within the projector augmented wave (PAW) formalism available in VASP.[111] The total energies of 128-atom and 104-atom supercells of Na_3PS_4 and Li_6PS_5X (X = I and Cl), respectively, are calculated with a plane-wave energy cutoff of 340 eV and a Γ-centered 4 × 4 × 4 Monkhorst pack k-point grid to sample the Brillouin zone. The positions of the ions in the defect supercells are relaxed following the procedure of refs 104, 112.

The elemental chemical potentials μ_i are expressed relative to those of the elements in reference elemental phases as $\mu_i = \mu_i^0 + \Delta\mu_i$, where μ_i^0 is the reference chemical potential under standard conditions and $\Delta\mu_i$ is the deviation from the reference. $\Delta\mu_i = 0$ corresponds to i-rich conditions. For example, $\Delta\mu_S = 0$ (S-rich) corresponds to the equilibrium between Li_6PS_5I and solid S. The reference chemical potentials (μ_i^0) are fitted to a set of measured formation enthalpies of compounds as in ref 113.

E_{corr} (eq 1) is estimated as in refs 59, 114 and contain: (i) the image charge correction for charged defects, (ii) the potential alignment correction for charged defects, (iii) the band filling correction for shallow defects, and (iv) the correction of the band edges for shallow acceptors/donors. The defect calculations were prepared and analyzed using pylada-defects software.[110]

The underestimation of the band gap in DFT is remedied by applying individual valence and conduction band edge shifts (relative to the DFT-computed band edges) as determined from GW quasiparticle energies.[59,70] We used DFT wave functions as input to the GW calculations. The GW eigenvalues are then iterated to self-consistency, removing the dependence on the single-particle energies of the initial DFT calculation. The input DFT wave functions are kept constant during the GW calculations, which allows the interpretation of the GW quasiparticle energies in terms of energy shifts relative to the Kohn–Sham energies. The GW quasiparticle energies are calculated using a Γ-centered 4 × 4 × 4 k-point grid for Na_3PS_4 and 6 × 4 × 4 grid for Li_6PS_5I and Li_6PS_5Cl. Under the given synthesis conditions, the equilibrium E_F is determined by solving the charge neutrality conditions, as discussed in Section 2.1.

6.3. Estimation of Carrier Mobility. To estimate the intrinsic carrier mobility (ζ) using eq 3, we need to compute the bulk modulus (B) and the band-effective mass (m_b^*) of the relevant bands—the conduction band for electrons and valence band for holes. m_b^* is calculated from the density-of-state (DOS) effective mass (m_{DOS}^*) and the band degeneracy (N_b) as in eq 4

$$m_b^* = N_b^{2/3} m_{DOS}^* \tag{4}$$

where we assumed parabolic bands and isotropic transport. The parabolic band approximation is used to extract m_{DOS}^* within a 100 meV energy window from the relevant band edge. B is determined by fitting the Birch–Murnaghan equation of state to a set of volumes and energies calculated with DFT for unit cells isotropically expanded and contracted around the equilibrium volume. The semiempirical model for the estimation of ζ (eq 3) is accurate within half an order of magnitude of experimental values,[48] which is satisfactory given that even measured ζ can exhibit orders of magnitude variations depending on the synthesis conditions and sample preparation.

6.4. Synthesis of Li_6PS_5X and Na_3PS_4. All samples were synthesized using solid-state synthesis routes starting from commercial binary reagents, i.e., Li_2S, Na_2S, P_2S_5, LiCl, or LiI. Stoichiometric mixtures of the appropriate reagents were prepared and pressed into pellets, which were subsequently sealed inside evacuated, carbon-coated quartz ampules. For the argyrodites, the ampules were heated to 550 °C in 10 h, held at that temperature for 48 h, and cooled back to room temperature at the same rate. For Na_3PS_4, the ampule was heated to 500 °C in 10 h, held for 20 h, and naturally cooled. All handling was performed in Ar-filled glove boxes.

Sample purity was verified with powder X-ray diffraction and Rietveld refinements as presented in Section S10 of the SI. Refinement results are in excellent agreement with previous experimental reports[60,90]

6.5. Ultraviolet-visible (UV–vis) spectroscopy. Diffuse-reflectance UV–vis spectra were collected using a custom setup composed of a deuterium arc lamp as a broadband light source and a QE65 Pro spectrometer (Ocean Optics). After optical focusing, light from the source was subsequently guided to the sample and the spectrometer using optical fiber bundles.

https://doi.org/10.1021/acs.chemmater.1c02345
Chem. Mater. XXXX, XXX, XXX–XXX

The samples were contained in custom hermetic sample holders featuring quartz windows. Barium sulfate ($BaSO_4$) powder was used as a reference. The spectra were interpreted using the Kubelka–Munk function and the Tauc method, as detailed in Section S8 of the SI.

■ ASSOCIATED CONTENT

Supporting Information

The Supporting Information is available free of charge at https://pubs.acs.org/doi/10.1021/acs.chemmater.1c02345.

Formation energetics of native defects of argyrodites and Na_3PS_4; phase equilibria of argyrodites and Na_3PS_4; provenance of the computed phases; ensemble statistic for modeling disordered argyrodites; band gap determination from UV–Vis spectra; an analysis of the deep defect states in argyrodites; the X-ray diffractograms of argyrodites and Na_3PS_4; and the band structures of the selected solid electrolytes (PDF)

■ AUTHOR INFORMATION

Corresponding Authors

Prashun Gorai − *Colorado School of Mines, Golden, Colorado 80401, United States;* orcid.org/0000-0001-7866-0672; Email: pgorai@mines.edu

Vladan Stevanović − *Colorado School of Mines, Golden, Colorado 80401, United States*; Email: vstevano@mines.edu

Pieremanuele Canepa − *Department of Materials Science and Engineering, National University of Singapore, Singapore 117575, Singapore; Singapore-MIT Alliance for Research and Technology, Singapore 138602, Singapore;* orcid.org/0000-0002-5168-9253; Email: pcanepa@nus.edu.sg

Authors

Theodosios Famprikis − *Storage of Electrochemical Energy, Faculty of Radiation Science and Technology, Delft University of Technology, Delft 2628, The Netherlands;* orcid.org/0000-0002-7946-1445

Baltej Singh − *Department of Materials Science and Engineering, National University of Singapore, Singapore 117575, Singapore; Department of Chemical and Biomolecular Engineering, National University of Singapore, Singapore 117585, Singapore*

Complete contact information is available at: https://pubs.acs.org/10.1021/acs.chemmater.1c02345

Notes

The authors declare no competing financial interest.

■ ACKNOWLEDGMENTS

P.C. is grateful to the ANR-NRF NRF2019-NRF-ANR073 Na-MASTER. P.C. acknowledges funding from the National Research Foundation under his NRF Fellowship NRFF12-2020-0012. P.C. is grateful to the Green Energy program under the project code R284-000-185-731. The computational work was performed on resources of the National Supercomputing Centre, Singapore (https://www.nscc.sg). The research was partly performed using computational resources sponsored by the Department of Energy's Office of Energy Efficiency and Renewable Energy and located at the National Renewable Energy Laboratory. The authors are thankful to Frédéric Sauvage for help with preliminary UV–Vis spectral measurements and analysis.

■ REFERENCES

(1) Tarascon, J.-M. Is lithium the new gold? *Nat. Chem.* **2010**, *2*, 510.

(2) Dunn, B.; Kamath, H.; Tarascon, J.-M. Electrical Energy Storage for the Grid: A Battery of Choices. *Science* **2011**, *334*, 928–935.

(3) Nykvist, B.; Nilsson, M. Rapidly falling costs of battery packs for electric vehicles. *Nat. Clim. Change* **2015**, *5*, 329–332.

(4) Larcher, D.; Tarascon, J.-M. Towards greener and more sustainable batteries for electrical energy storage. *Nat. Chem.* **2015**, *7*, 19–29.

(5) Cano, Z. P.; Banham, D.; Ye, S.; Hintennach, A.; Lu, J.; Fowler, M.; Chen, Z. Batteries and fuel cells for emerging electric vehicle markets. *Nat. Energy* **2018**, *3*, 279–289.

(6) Crabtree, G. The coming electric vehicle transformation. *Science* **2019**, *366*, 422–424.

(7) Zhang, S. S. A review on the separators of liquid electrolyte Li-ion batteries. *J. Power Sources* **2007**, *164*, 351–364.

(8) Yoo, H. D.; Markevich, E.; Salitra, G.; Sharon, D.; Aurbach, D. On the challenge of developing advanced technologies for electrochemical energy storage and conversion. *Mater. Today* **2014**, *17*, 110–121.

(9) Liu, K.; Liu, Y.; Lin, D.; Pei, A.; Cui, Y. Materials for lithium-ion battery safety. *Sci. Adv.* **2018**, *4*, No. eaas9820.

(10) Goodenough, J. B.; Kim, Y. Challenges for Rechargeable Li Batteries†. *Chem. Mater.* **2010**, *22*, 587–603.

(11) Peled, E. The Electrochemical Behavior of Alkali and Alkaline Earth Metals in Nonaqueous Battery Systems—The Solid Electrolyte Interphase Model. *J. Electrochem. Soc.* **1979**, *126*, 2047.

(12) Rao, R. P.; Adams, S. Studies of lithium argyrodite solid electrolytes for all-solid-state batteries. *Phys. Status Solidi A* **2011**, *208*, 1804–1807.

(13) Tatsumisago, M.; Hayashi, A. Superionic glasses and glass–ceramics in the $Li2_S$–P_2S_5 system for all-solid-state lithium secondary batteries. *Solid State Ionics* **2012**, *225*, 342–345.

(14) Tatsumisago, M.; Nagao, M.; Hayashi, A. Recent development of sulfide solid electrolytes and interfacial modification for all-solid-state rechargeable lithium batteries. *J. Asian Ceram. Soc.* **2013**, *1*, 17–25.

(15) Bachman, J. C.; Muy, S.; Grimaud, A.; Chang, H.-H.; Pour, N.; Lux, S. F.; Paschos, O.; Maglia, F.; Lupart, S.; Lamp, P.; Giordano, L.; Shao-Horn, Y. Inorganic Solid-State Electrolytes for Lithium Batteries: Mechanisms and Properties Governing Ion Conduction. *Chem. Rev.* **2016**, *116*, 140–162.

(16) Janek, J.; Zeier, W. G. A solid future for battery development. *Nat. Energy* **2016**, *1*, No. 16141.

(17) Famprikis, T.; Canepa, P.; Dawson, J. A.; Islam, M. S.; Masquelier, C. Fundamentals of inorganic solid-state electrolytes for batteries. *Nat. Mater.* **2019**, *18*, 1278–1291.

(18) Kamaya, N.; Homma, K.; Yamakawa, Y.; Hirayama, M.; Kanno, R.; Yonemura, M.; Kamiyama, T.; Kato, Y.; Hama, S.; Kawamoto, K.; Mitsui, A. A lithium superionic conductor. *Nat. Mater.* **2011**, *10*, 682–686.

(19) Rayavarapu, P. R.; Sharma, N.; Peterson, V. K.; Adams, S. Variation in structure and Li^+-ion migration in argyrodite-type Li_6PS_5X (X = Cl, Br, I) solid electrolytes. *J. Solid State Electrochem.* **2012**, *16*, 1807–1813.

(20) Adams, S.; Rao, R. P. Structural requirements for fast lithium ion migration in $Li_{10}GeP_2S_{12}$. *J. Mater. Chem.* **2012**, *22*, 7687.

(21) Kato, Y.; Hori, S.; Saito, T.; Suzuki, K.; Hirayama, M.; Mitsui, A.; Yonemura, M.; Iba, H.; Kanno, R. High-power all-solid-state batteries using sulfide superionic conductors. *Nat. Energy* **2016**, *1*, No. 16030.

(22) Gao, Y.; Nolan, A. M.; Du, P.; Wu, Y.; Yang, C.; Chen, Q.; Mo, Y.; Bo, S.-H. Classical and Emerging Characterization Techniques for Investigation of Ion Transport Mechanisms in Crystalline Fast Ionic Conductors. *Chem. Rev.* **2020**, 5954.

(23) Logan, E.; Dahn, J. Electrolyte Design for Fast-Charging Li-Ion Batteries. *Trends Chem.* **2020**, *2*, 354−366.
(24) Zhu, Y.; He, X.; Mo, Y. Origin of Outstanding Stability in the Lithium Solid Electrolyte Materials: Insights from Thermodynamic Analyses Based on First-Principles Calculations. *ACS Appl. Mater. Interfaces* **2015**, *7*, 23685−23693.
(25) Richards, W. D.; Miara, L. J.; Wang, Y.; Kim, J. C.; Ceder, G. Interface Stability in Solid-State Batteries. *Chem. Mater.* **2016**, *28*, 266−273.
(26) Auvergniot, J.; Cassel, A.; Ledeuil, J.-B.; Viallet, V.; Seznec, V.; Dedryvére, R. Interface Stability of Argyrodite Li_6PS_5Cl toward $LiCoO_2$, $LiNi_{1/3}Co_{1/3}Mn_{1/3}O_2$, and $LiMn_2O_4$ in Bulk All-Solid-State Batteries. *Chem. Mater.* **2017**, *29*, 3883−3890.
(27) Koerver, R.; Zhang, W.; de Biasi, L.; Schweidler, S.; Kondrakov, A. O.; Kolling, S.; Brezesinski, T.; Hartmann, P.; Zeier, W. G.; Janek, J. Chemo-mechanical expansion of lithium electrode materials − on the route to mechanically optimized all-solid-state batteries. *Energy Environ. Sci.* **2018**, *11*, 2142−2158.
(28) Butler, K. T.; Gautam, G. S.; Canepa, P. Designing interfaces in energy materials applications with first-principles calculations. *npj Comput. Mater.* **2019**, *5*, No. 19.
(29) Kasemchainan, J.; Zekoll, S.; Jolly, D. S.; Ning, Z.; Hartley, G. O.; Marrow, J.; Bruce, P. G. Critical stripping current leads to dendrite formation on plating in lithium anode solid electrolyte cells. *Nat. Mater.* **2019**, *18*, 1105−1111.
(30) Schwietert, T. K.; Arszelewska, V. A.; Wang, C.; Yu, C.; Vasileiadis, A.; de Klerk, N. J. J.; Hageman, J.; Hupfer, T.; Kerkamm, I.; Xu, Y.; van der Maas, E.; Kelder, E. M.; Ganapathy, S.; Wagemaker, M. Clarifying the relationship between redox activity and electrochemical stability in solid electrolytes. *Nat. Mater.* **2020**, *19*, 428−435.
(31) Deng, Z.; Gautam, G. S.; Kolli, S. K.; Chotard, J.-N.; Cheetham, A. K.; Masquelier, C.; Canepa, P. Phase Behavior in Rhombohedral NaSiCON Electrolytes and Electrodes. *Chem. Mater.* **2020**, *32*, 7908−7920.
(32) Yu, C.; Ganapathy, S.; van Eck, E. R. H.; Wang, H.; Basak, S.; Li, Z.; Wagemaker, M. Accessing the bottleneck in all-solid state batteries, lithium-ion transport over the solid-electrolyte-electrode interface. *Nat. Commun.* **2017**, *8*, No. 1086.
(33) Porz, L.; Swamy, T.; Sheldon, B. W.; Rettenwander, D.; Frömling, T.; Thaman, H. L.; Berendts, S.; Uecker, R.; Carter, W. C.; Chiang, Y.-M. Mechanism of Lithium Metal Penetration through Inorganic Solid Electrolytes. *Adv. Energy Mater.* **2017**, *7*, No. 1701003.
(34) Cheng, E. J.; Sharafi, A.; Sakamoto, J. Intergranular Li metal propagation through polycrystalline $Li_{6.25}Al_{0.25}La_3Zr_2O_{12}$ ceramic electrolyte. *Electrochim. Acta* **2017**, *223*, 85−91.
(35) Marbella, L. E.; Zekoll, S.; Kasemchainan, J.; Emge, S. P.; Bruce, P. G.; Grey, C. P. ^{7}Li NMR Chemical Shift Imaging To Detect Microstructural Growth of Lithium in All-Solid-State Batteries. *Chem. Mater.* **2019**, *31*, 2762−2769.
(36) Han, F.; Westover, A. S.; Yue, J.; Fan, X.; Wang, F.; Chi, M.; Leonard, D. N.; Dudney, N. J.; Wang, H.; Wang, C. High electronic conductivity as the origin of lithium dendrite formation within solid electrolytes. *Nat. Energy* **2019**, *4*, 187−196.
(37) Song, Y.; Yang, L.; Tao, L.; Zhao, Q.; Wang, Z.; Cui, Y.; Liu, H.; Lin, Y.; Pan, F. Probing into the origin of an electronic conductivity surge in a garnet solid-state electrolyte. *J. Mater. Chem. A* **2019**, *7*, 22898−22902.
(38) Krauskopf, T.; Richter, F. H.; Zeier, W. G.; Janek, J. Physicochemical Concepts of the Lithium Metal Anode in Solid-State Batteries. *Chem. Rev.* **2020**, *120*, 7745−7794.
(39) Boulineau, S.; Courty, M.; Tarascon, J.-M.; Viallet, V. Mechanochemical synthesis of Li-argyrodite Li6PS5X (X = Cl, Br, I) as sulfur-based solid electrolytes for all solid state batteries application. *Solid State Ionics* **2012**, *221*, 1−5.
(40) Wenzel, S.; Randau, S.; Leichtweiß, T.; Weber, D. A.; Sann, J.; Zeier, W. G.; Janek, J. Direct Observation of the Interfacial Instability of the Fast Ionic Conductor $Li_{10}GeP_2S_{12}$ at the Lithium Metal Anode. *Chem. Mater.* **2016**, *28*, 2400−2407.
(41) Philipp, M.; Gadermaier, B.; Posch, P.; Hanzu, I.; Ganschow, S.; Meven, M.; Rettenwander, D.; Redhammer, G. J.; Wilkening, H. M. R. The Electronic Conductivity of Single Crystalline Ga-Stabilized Cubic $Li_7La_3Zr_2O_{12}$: A Technologically Relevant Parameter for All-Solid-State Batteries. *Adv. Mater. Interfaces* **2020**, No. 2000450.
(42) Thompson, T.; Yu, S.; Williams, L.; Schmidt, R. D.; Garcia-Mendez, R.; Wolfenstine, J.; Allen, J. L.; Kioupakis, E.; Siegel, D. J.; Sakamoto, J. Electrochemical Window of the Li-Ion Solid Electrolyte $Li_7La_3Zr_2O_{12}$. *ACS Energy Lett.* **2017**, *2*, 462−468.
(43) Chen, S.; Wu, C.; Shen, L.; Zhu, C.; Huang, Y.; Xi, K.; Maier, J.; Yu, Y. Challenges and Perspectives for NASICOn-type Electrode Materials for Advanced Sodium-Ion Batteries. *Adv. Mater.* **2017**, *29*, No. 1700431.
(44) Zhou, L.; Park, K.-H.; Sun, X.; Lalére, F.; Adermann, T.; Hartmann, P.; Nazar, L. F. Solvent-Engineered Design of Argyrodite Li_6PS_5X (X = Cl, Br, I) Solid Electrolytes with High Ionic Conductivity. *ACS Energy Lett.* **2018**, *4*, 265−270.
(45) Deiseroth, H.-J.; Maier, J.; Weichert, K.; Nickel, V.; Kong, S.-T.; Reiner, C. Li_7PS_6 and Li_6PS_5X (X: Cl, Br, I): Possible Three-dimensional Diffusion Pathways for Lithium Ions and Temperature Dependence of the Ionic Conductivity by Impedance Measurements. *Z. Anorg. Allg. Chem.* **2011**, *637*, 1287−1294.
(46) Minami, K.; Mizuno, F.; Hayashi, A.; Tatsumisago, M. Lithium ion conductivity of the Li_2S-P_2S_5 glass-based electrolytes prepared by the melt quenching method. *Solid State Ionics* **2007**, *178*, 837−841.
(47) Shin, B. R.; Nam, Y. J.; Oh, D. Y.; Kim, D. H.; Kim, J. W.; Jung, Y. S. Comparative Study of TiS_2 /Li-In All-Solid-State Lithium Batteries Using Glass-Ceramic Li_3PS_4 and $Li_{10}GeP_2S_{12}$ Solid Electrolytes. *Electrochim. Acta* **2014**, *146*, 395−402.
(48) Yan, J.; Gorai, P.; Ortiz, B.; Miller, S.; Barnett, S. A.; Mason, T.; Stevanović, V.; Toberer, E. S. Material descriptors for predicting thermoelectric performance. *Energy Environ. Sci.* **2015**, *8*, 983−994.
(49) Ong, S. P.; Chevrier, V. L.; Hautier, G.; Jain, A.; Moore, C.; Kim, S.; Ma, X.; Ceder, G. Voltage, stability and diffusion barrier differences between sodium-ion and lithium-ion intercalation materials. *Energy Environ. Sci.* **2011**, *4*, 3680.
(50) Kim, S.-W.; Seo, D.-H.; Ma, X.; Ceder, G.; Kang, K. Electrode Materials for Rechargeable Sodium-Ion Batteries: Potential Alternatives to Current Lithium-Ion Batteries. *Adv. Energy Mater.* **2012**, *2*, 710−721.
(51) Masquelier, C.; Croguennec, L. Polyanionic (Phosphates, Silicates, Sulfates) Frameworks as Electrode Materials for Rechargeable Li (or Na) Batteries. *Chem. Rev.* **2013**, *113*, 6552−6591.
(52) Yabuuchi, N.; Kubota, K.; Dahbi, M.; Komaba, S. Research Development on Sodium-Ion Batteries. *Chem. Rev.* **2014**, *114*, 11636−11682.
(53) Chu, I.-H.; Kompella, C. S.; Nguyen, H.; Zhu, Z.; Hy, S.; Deng, Z.; Meng, Y. S.; Ong, S. P. Room-Temperature All-solid-state Rechargeable Sodium-ion Batteries with a Cl-doped Na3PS4 Superionic Conductor. *Sci. Rep.* **2016**, *6*, No. 33733.
(54) McCluskey, M. D.; Haller, E. E. *Dopants and Defects in Semiconductors*; CRC Press, 2018.
(55) Canepa, P.; Gautam, G. S.; Broberg, D.; Bo, S.-H.; Ceder, G. Role of Point Defects in Spinel Mg Chalcogenide Conductors. *Chem. Mater.* **2017**, *29*, 9657−9667.
(56) Gorai, P.; Long, H.; Jones, E.; Santhanagopalan, S.; Stevanović, V. Defect chemistry of disordered solid-state electrolyte $Li_{10}GeP_2S_{12}$. *J. Mater. Chem. A* **2020**, *8*, 3851−3858.
(57) Oh, K.; Chang, D.; Lee, B.; Kim, D.-H.; Yoon, G.; Park, I.; Kim, B.; Kang, K. Native Defects in $Li_{10}GeP_2S_{12}$ and Their Effect on Lithium Diffusion. *Chem. Mater.* **2018**, *30*, 4995−5004.
(58) Smith, J. G.; Naruse, J.; Hiramatsu, H.; Siegel, D. J. Intrinsic Conductivity in Magnesium-Oxygen Battery Discharge Products: MgO and MgO_2. *Chem. Mater.* **2017**, *29*, 3152−3163.
(59) Lany, S.; Zunger, A. Assessment of Correction Methods for the Band-gap Problem and for Finite-size Effects in Supercell Defect Calculations: Case Studies for ZnO and GaAs. *Phys. Rev. B* **2008**, *78*, No. 235104.

https://doi.org/10.1021/acs.chemmater.1c02345
Chem. Mater. XXXX, XXX, XXX−XXX

(60) Kraft, M. A.; Culver, S. P.; Calderon, M.; Böcher, F.; Krauskopf, T.; Senyshyn, A.; Dietrich, C.; Zevalkink, A.; Janek, J.; Zeier, W. G. Influence of Lattice Polarizability on the Ionic Conductivity in the Lithium Superionic Argyrodites Li_6PS_5X (X = Cl, Br, I). *J. Am. Chem. Soc.* **2017**, *139*, 10909−10918.
(61) Krauskopf, T.; Culver, S. P.; Zeier, W. G. Local Tetragonal Structure of the Cubic Superionic Conductor Na_3PS_4. *Inorg. Chem.* **2018**, *57*, 4739−4744.
(62) Squires, A.; Davies, D.; Kim, S.; Scanlon, D.; Walsh, A.; Morgan, B. Low Electronic Conductivity of Li7La3Zr2O12 (LLZO) Solid Electrolytes from First Principles. ChemRxiv. 2020. (accessed on 20th Aug 2021). https://doi.org/10.33774/chemrxiv-2021-zvwhh-v2.
(63) Ashcroft, N. W.; Mermin, N. D. et al. *Solid State Physics*; Harcourt College Publishers: Orlando, 1976.
(64) Giustino, F. Electron-phonon interactions from first principles. *Rev. Mod. Phys.* **2017**, *89*, No. 015003.
(65) Dietrich, C.; Weber, D. A.; Culver, S.; Senyshyn, A.; Sedlmaier, S. J.; Indris, S.; Janek, J.; Zeier, W. G. Synthesis, Structural Characterization, and Lithium Ion Conductivity of the Lithium Thiophosphate $Li_2P_2S_6$. *Inorg. Chem.* **2017**, *56*, 6681−6687.
(66) Wenzel, S.; Sedlmaier, S. J.; Dietrich, C.; Zeier, W. G.; Janek, J. Interfacial reactivity and interphase growth of argyrodite solid electrolytes at lithium metal electrodes. *Solid State Ionics* **2018**, *318*, 102−112.
(67) Krauskopf, T.; Culver, S. P.; Zeier, W. G. Bottleneck of Diffusion and Inductive Effects in $Li_{10}Ge_{1-x}Sn_xP_2S_{12}$. *Chem. Mater.* **2018**, *30*, 1791−1798.
(68) Culver, S. P.; Squires, A. G.; Minafra, N.; Armstrong, C. W. F.; Krauskopf, T.; Böcher, F.; Li, C.; Morgan, B. J.; Zeier, W. G. Evidence for a Solid-Electrolyte Inductive Effect in the Superionic Conductor $Li_{10}Ge_{1-x}Sn_xP_2S_{12}$. *J. Am. Chem. Soc.* **2020**, *142*, 21210−21219.
(69) Strauss, F.; Zinkevich, T.; Indris, S.; Brezesinski, T. Li_7GeS_5Br—An Argyrodite Li-Ion Conductor Prepared by Mechanochemical Synthesis. *Inorg. Chem.* **2020**, *59*, 12954−12959.
(70) Peng, H.; Scanlon, D. O.; Stevanovic, V.; Vidal, J.; Watson, G. W.; Lany, S. Convergence of density and hybrid functional defect calculations for compound semiconductors. *Phys. Rev. B* **2013**, *88*, No. 115201.
(71) Seo, D.-H.; Urban, A.; Ceder, G. Calibrating transition-metal energy levels and oxygen bands in first-principles calculations: Accurate prediction of redox potentials and charge transfer in lithium transition-metal oxides. *Phys. Rev. B* **2015**, *92*, No. 115118.
(72) Kotani, T.; van Schilfgaarde, M.; Faleev, S. V. Quasiparticle self-consistent GW method: A basis for the independent-particle approximation. *Phys. Rev. B* **2007**, *76*, No. 165106.
(73) van Schilfgaarde, M.; Kotani, T.; Faleev, S. Quasiparticle Self-Consistent *GW* Theory. *Phys. Rev. Lett.* **2006**, *96*, No. 226402.
(74) Hüser, F.; Olsen, T.; Thygesen, K. S. Quasiparticle GW calculations for solids, molecules, and two-dimensional materials. *Phys. Rev. B* **2013**, *87*, No. 235132.
(75) Kong, S. Dissertation. Ph.D. Thesis, Universität Siegen, 2010.
(76) Perdew, J. P.; Burke, K.; Ernzerhof, M. Generalized Gradient Approximation Made Simple. *Phys. Rev. Lett.* **1996**, *77*, 3865.
(77) Gautam, A.; Sadowski, M.; Prinz, N.; Eickhoff, H.; Minafra, N.; Ghidiu, M.; Culver, S. P.; Albe, K.; Fässler, T. F.; Zobel, M.; Zeier, W. G. Rapid Crystallization and Kinetic Freezing of Site-Disorder in the Lithium Superionic Argyrodite Li_6PS_5Br. *Chem. Mater.* **2019**, *31*, 10178−10185.
(78) Hanghofer, I.; Brinek, M.; Eisbacher, S. L.; Bitschnau, B.; Volck, M.; Hennige, V.; Hanzu, I.; Rettenwander, D.; Wilkening, H. M. R. Substitutional disorder: structure and ion dynamics of the argyrodites Li_6PS_5Cl, Li_6PS_5Br and Li_6PS_5I. *Phys. Chem. Chem. Phys.* **2019**, *21*, 8489−8507.
(79) Nguyen, H.; Banerjee, A.; Wang, X.; Tan, D.; Wu, E. A.; Doux, J.-M.; Stephens, R.; Verbist, G.; Meng, Y. S. Single-step synthesis of highly conductive Na_3PS_4 solid electrolyte for sodium all solid-state batteries. *J. Power Sources* **2019**, *435*, No. 126623.
(80) Mukhopadhyay, S.; Thompson, T.; Sakamoto, J.; Huq, A.; Wolfenstine, J.; Allen, J. L.; Bernstein, N.; Stewart, D. A.; Johannes, M. D. Structure and Stoichiometry in Supervalent Doped $Li_7La_3Zr_2O_{12}$. *Chem. Mater.* **2015**, *27*, 3658−3665.
(81) Squires, A. G.; Scanlon, D. O.; Morgan, B. J. Native Defects and Their Doping Response in the Lithium Solid Electrolyte $Li_7La_3Zr_2O_{12}$. *Chem. Mater.* **2019**, *32*, 1876−1886.
(82) Sharafi, A.; Haslam, C. G.; Kerns, R. D.; Wolfenstine, J.; Sakamoto, J. Controlling and correlating the effect of grain size with the mechanical and electrochemical properties of $Li_7La_3Zr_2O_{12}$ solid-state electrolyte. *J. Mater. Chem. A* **2017**, *5*, 21491−21504.
(83) Canepa, P.; Dawson, J. A.; Gautam, G. S.; Statham, J. M.; Parker, S. C.; Islam, M. S. Particle Morphology and Lithium Segregation to Surfaces of the $Li_7La_3Zr_2O_{12}$ Solid Electrolyte. *Chem. Mater.* **2018**, *30*, 3019−3027.
(84) Dawson, J. A.; Canepa, P.; Famprikis, T.; Masquelier, C.; Islam, M. S. Atomic-Scale Influence of Grain Boundaries on Li-Ion Conduction in Solid Electrolytes for All-Solid-State Batteries. *J. Am. Chem. Soc.* **2018**, *140*, 362−368.
(85) Dawson, J. A.; Canepa, P.; Clarke, M. J.; Famprikis, T.; Ghosh, D.; Islam, M. S. Toward Understanding the Different Influences of Grain Boundaries on Ion Transport in Sulfide and Oxide Solid Electrolytes. *Chem. Mater.* **2019**, *31*, 5296−5304.
(86) Banik, A.; Famprikis, T.; Ghidiu, M.; Ohno, S.; Kraft, M. A.; Zeier, W. G. On the underestimated influence of synthetic conditions in solid ionic conductors. *Chem. Sci.* **2021**, *12*, 6238−6263.
(87) Moran, R. F.; McKay, D.; Tornstrom, P. C.; Aziz, A.; Fernandes, A.; Grau-Crespo, R.; Ashbrook, S. E. Ensemble-Based Modeling of the NMR Spectra of Solid Solutions: Cation Disorder in $Y_2(Sn,Ti)_2O_7$. *J. Am. Chem. Soc.* **2019**, *141*, 17838.
(88) Jones, E.; Stevanovic, V. The Glassy Solid as a Statistical Ensemble of Crystalline Microstates. *npJ Comput. Mater.* **2020**, *6*, No. 56.
(89) Zhang, Z.; Shao, Y.; Lotsch, B.; Hu, Y.-S.; Li, H.; Janek, J.; Nazar, L. F.; Nan, C.-W.; Maier, J.; Armand, M.; Chen, L. New horizons for inorganic solid state ion conductors. *Energy Environ. Sci.* **2018**, *11*, 1945−1976.
(90) Famprikis, T.; et al. Under Pressure: Mechanochemical Effects on Structure and Ion Conduction in the Sodium-Ion Solid Electrolyte Na_3PS_4. *J. Am. Chem. Soc.* **2020**, *142*, 18422−18436.
(91) Minafra, N.; Kraft, M. A.; Bernges, T.; Li, C.; Schlem, R.; Morgan, B. J.; Zeier, W. G. Local Charge Inhomogeneity and Lithium Distribution in the Superionic Argyrodites Li_6PS_5X (X = Cl, Br, I). *Inorg. Chem.* **2020**, *59*, 11009−11019.
(92) Gautam, A.; Sadowski, M.; Ghidiu, M.; Minafra, N.; Senyshyn, A.; Albe, K.; Zeier, W. G. Engineering the Site-Disorder and Lithium Distribution in the Lithium Superionic Argyrodite Li_6PS_5Br. *Adv. Energy Mater.* **2020**, *11*, No. 2003369.
(93) Stegmaier, S.; Voss, J.; Reuter, K.; Luntz, A. C. Li^+ Defects in a Solid-State Li Ion Battery: Theoretical Insights with a Li_3OCl Electrolyte. *Chem. Mater.* **2017**, *29*, 4330−4340.
(94) Cardona, M.; Peter, Y. Y. *Fundamentals of Semiconductors*; Springer, 2005.
(95) Riess, I. Review of the limitation of the Hebb-Wagner polarization method for measuring partial conductivities in mixed ionic electronic conductors. *Solid State Ionics* **1996**, *91*, 221−232.
(96) Riess, I. Application of the van der Pauw method to conductivity measurements on mixed ionic-electronic solid conductors. *Solid State Ionics* **1982**, *7*, 307−315.
(97) Borup, K. A.; de Boor, J.; Wang, H.; Drymiotis, F.; Gascoin, F.; Shi, X.; Chen, L.; Fedorov, M. I.; Müller, E.; Iversen, B. B.; Snyder, G. J. Measuring thermoelectric transport properties of materials. *Energy Environ. Sci.* **2015**, *8*, 423−435.
(98) Kumar, P.; Repaka, D. V. M.; Hippalgaonkar, K. Lithography-free resistance thermometry based technique to accurately measure Seebeck coefficient and electrical conductivity for organic and inorganic thin films. *Rev. Sci. Instrum.* **2017**, *88*, No. 125112.

(99) Zevalkink, A.; et al. A practical field guide to thermoelectrics: Fundamentals, synthesis, and characterization. *Appl. Phys. Rev.* **2018**, *5*, No. 021303.
(100) Wei, T.-R.; Guan, M.; Yu, J.; Zhu, T.; Chen, L.; Shi, X. How to Measure Thermoelectric Properties Reliably. *Joule* **2018**, *2*, 2183−2188.
(101) Trudeau, M. L.; Schulz, R.; Dussault, D.; Neste, A. V. Structural changes during high-energy ball milling of iron-based amorphous alloys: Is high-energy ball milling equivalent to a thermal process? *Phys. Rev. Lett.* **1990**, *64*, 99−102.
(102) Koch, C. Synthesis of nanostructured materials by mechanical milling: problems and opportunities. *Nanostruct. Mater.* **1997**, *9*, 13−22.
(103) Šepelák, V.; Bégin-Colin, S.; Caër, G. L. Transformations in oxides induced by high-energy ball-milling. *Dalton Trans.* **2012**, *41*, 11927.
(104) Ohno, S.; Imasato, K.; Anand, S.; Tamaki, H.; Kang, S. D.; Gorai, P.; Sato, H. K.; Toberer, E. S.; Kanno, T.; Snyder, G. J. Phase Boundary Mapping to Obtain n-type Mg_3Sb_2-based Thermoelectrics. *Joule* **2018**, *2*, 141.
(105) Aykol, M.; Kim, S.; Hegde, V. I.; Snydacker, D.; Lu, Z.; Hao, S.; Kirklin, S.; Morgan, D.; Wolverton, C. High-throughput computational design of cathode coatings for Li-ion batteries. *Nat. Commun.* **2016**, *7*, No. 13779.
(106) Xiao, Y.; Wang, Y.; Bo, S.-H.; Kim, J. C.; Miara, L. J.; Ceder, G. Understanding interface stability in solid-state batteries. *Nat. Rev. Mater.* **2020**, *5*, 105−126.
(107) Xiao, Y.; Miara, L. J.; Wang, Y.; Ceder, G. Computational Screening of Cathode Coatings for Solid-State Batteries. *Joule* **2019**, *3*, 1252−1275.
(108) Culver, S. P.; Koerver, R.; Zeier, W. G.; Janek, J. On the Functionality of Coatings for Cathode Active Materials in Thiophosphate-Based All-Solid-State Batteries. *Adv. Energy Mater.* **2019**, *9*, No. 1900626.
(109) Hart, G. L. W.; Forcade, R. W. Algorithm for generating derivative structures. *Phys. Rev. B* **2008**, *77*, No. 224115.
(110) Goyal, A.; Gorai, P.; Peng, H.; Lany, S.; Stevanović, V. S. A Computational Framework for Automation of Point Defect Calculations. *Comput. Mater. Sci.* **2017**, *130*, 1.
(111) Kresse, G.; Furthmüller, J. Efficient Iterative Schemes for ab initio Total-energy Calculations Using a Plane-wave Basis Set. *Phys. Rev. B* **1996**, *54*, 11169.
(112) Gorai, P.; Ortiz, B.; Toberer, E. S.; Stevanovic, V. Investigation of n-type Doping Strategies for Mg_3Sb_2. *J. Mater. Chem. A* **2018**, *6*, 13806.
(113) Stevanović, V.; Lany, S.; Zhang, X.; Zunger, A. Correcting density functional theory for accurate predictions of compound enthalpies of formation: Fitted elemental-phase reference energies. *Phys. Rev. B* **2012**, *85*, No. 115104.
(114) Freysoldt, C.; Grabowski, B.; Hickel, T.; Neugebauer, J.; Kresse, G.; Janotti, A.; de Walle, C. G. V. First-principles calculations for point defects in solids. *Rev. Mod. Phys.* **2014**, *86*, 253−305.

https://doi.org/10.1021/acs.chemmater.1c02345
Chem. Mater. XXXX, XXX, XXX−XXX